**Key Points:**

- A modeling framework from the terrestrial surface energy budget perspective is used to investigate aerosol-climate interactions
- Aerosols enhance primary productivity and reduce terrestrial Bowen ratio, causing evaporative cooling over vegetated surfaces
- Diffuse radiation fertilization effect is important for primary productivity while global dimming controls the evaporative cooling

**Author Contributions:**

**Conceptualization:** TC Chakraborty, Xuhui Lee
**Formal analysis:** TC Chakraborty
**Investigation:** TC Chakraborty
**Methodology:** TC Chakraborty, Xuhui Lee, David M. Lawrence
**Visualization:** TC Chakraborty
**Writing – original draft:** TC Chakraborty, Xuhui Lee

# Strong Local Evaporative Cooling Over Land Due to Atmospheric Aerosols

**TC Chakraborty[1]** , **Xuhui Lee[1]** , **and David M. Lawrence[2]**

[1]School of the Environment, Yale University, New Haven, CT, USA, [2]National Center for Atmospheric Research, Boulder, CO, USA

**Abstract** Aerosols can enhance terrestrial productivity through increased absorption of solar radiation by the shaded portion of the plant canopy—the diffuse radiation fertilization effect. Although this process can, in principle, alter surface evaporation due to the coupling between plant water loss and carbon uptake, with the potential to change the surface temperature, aerosol-climate interactions have been traditionally viewed in light of the radiative effects within the atmosphere. Here, we develop a modeling framework that combines global atmosphere and land model simulations with a conceptual diagnostic tool to investigate these interactions from a surface energy budget perspective. Aerosols increase the terrestrial evaporative fraction, or the portion of net incoming energy consumed by evaporation, by over 4% globally and as much as ~40% regionally. The main mechanism for this is the increase in energy allocation from sensible to latent heat due to global dimming (reduction in global shortwave radiation) and slightly augmented by diffuse radiation fertilization. In regions with moderately dense vegetation (leaf area index >2), the local surface cooling response to aerosols is dominated by this evaporative pathway, not the reduction in incident radiation. Diffuse radiation fertilization alone has a stronger impact on gross primary productivity (+2.18 Pg C y$^{-1}$ or +1.8%) than on land evaporation (+0.18 W m$^{-2}$ or +0.48%) and surface temperature (−0.01 K). Our results suggest that it is important for land surface models to distinguish between quantity (change in total magnitude) and quality (change in diffuse fraction) of radiative forcing for properly simulating surface climate.

**Plain Language Summary** Atmospheric particles or aerosols are known to enhance plant growth by increasing photosynthesis in leaves that are normally shaded from direct sunlight, a phenomenon known as the diffuse radiation fertilization effect. Since photosynthesis and water vapor released from plants are linked, this would imply that there is more evaporative cooling at the surface under polluted skies, a mechanism of aerosol-induced cooling that has not been explicitly considered in past studies. In the present study, we test this hypothesis on a global scale by combining a modeling framework with an offline energy balance method. We show that the surface cooling due to the evaporative pathway is stronger than due to the radiative effect of aerosols for moderately dense vegetation. Traditionally, aerosol-climate interactions are viewed in light of their radiation impacts on the atmospheric energy budget. Our study provides a new, surface energy budget perspective on these interactions and highlight the importance of differentiating between the quantity and quality of radiative forcing at the Earth's surface when examining the impact of aerosols on the surface climate.

## 1. Introduction

Aerosols modify the Earth's radiative budget through scattering and absorption of solar (shortwave) and terrestrial (longwave) radiation and have large variability in their physical and chemical properties, horizontal and vertical distributions, and feedbacks from other components of the climate system, particularly clouds (Persad & Caldeira, 2018; Ramanathan, 2001). Overall, aerosol climatic effects lead to one of the largest uncertainties in future climate projections (Hinds, 1999; Stocker, 2014). Unlike the effect of well-mixed greenhouse gases, the aerosol radiative effect is stronger at the surface than at the top of the atmosphere (Ramanathan, 2001), with aerosols reducing incoming shortwave radiation through scattering and absorption and increasing incoming longwave radiation through re-emission of the absorbed energy (Chakraborty & Lee, 2019; Panicker et al., 2008).

**Writing – review & editing:** Xuhui Lee, David M. Lawrence

Several past studies have examined the aerosol climatic impacts through the lens of atmospheric energy balance (Chung et al., 2005; Persad & Caldeira, 2018; Ramanathan, 2001). In this study, we aim to investigate the global impacts of aerosols from a terrestrial surface energy budget perspective. One outstanding question concerns how the surface sensible heat ($H$) and latent heat flux ($\lambda E$) respond differently to the aerosol surface radiative effect. Both regional modeling and observational studies show that aerosols may reduce $H$ more than $\lambda E$, resulting in an increase of the evaporative fraction (EF), or the proportion of net incoming energy at the surface dissipated through evaporation (Knohl & Baldocchi, 2008; Liu et al., 2014; Matsui et al., 2008; Steiner et al., 2013; S. Wang et al., 2018; W. Wang et al., 2018; Zhang et al., 2008). Two competing hypotheses are advanced to explain the enhanced EF. First, aerosols alter quality of the shortwave radiation by increasing diffuse radiation ($K_{\downarrow,d}$) at the Earth's surface, which can penetrate deeper into the canopy than direct or beam solar radiation and illuminates normally light-limited portion of the vegetation (Gu et al., 2003). The resulting increase in primary productivity is called the diffuse radiation fertilization effect (Gu et al., 2002; Mercado et al., 2009; Niyogi et al., 2004; Rap et al., 2018, 2015). Since carbon uptake and water loss are coupled in plants through stomatal conductance, the primary hypothesis is that this increase in diffuse radiation modifies the moisture flux from the surface and therefore EF (K. Wang et al., 2008). A second hypothesis for the change in EF, implicit in the studies of Gu et al. (2006) and others (Oliveira et al., 2011), is that global dimming, or reduction in quantity of the surface shortwave radiation, is responsible for how the surface available energy is partitioned between $H$ and $\lambda E$. It is not known which of the two mechanisms—the diffuse radiation fertilization effect or the global dimming effect—dominates the EF response.

A second question of broad interest asks how temperatures respond to aerosol loading. Since the aerosol radiative effect is much larger at the surface than in the atmosphere or at the top of the atmosphere, it follows that aerosols disproportionately affect surface temperature ($T_s$; Chakraborty & Lee, 2019). A reduction in incoming radiation generally causes surface cooling, but the cooling signal is highly variable in space because land biophysical properties exert a strong control on this local climate response to atmospheric forcing (Bright et al., 2017; Luyssaert et al., 2014) and because the biophysical properties of the surface and the aerosol loading aloft tend to co-vary geographically (Chakraborty & Lee, 2019). In addition, changes in non-radiative processes like convection, evaporation and EF can change $T_s$, even under a constant amount of incoming radiation (Bonan, 2008; Lee et al., 2011). A recent study has examined the $T_s$ response to the direct radiative effect (Chakraborty & Lee, 2019). How aerosols modify $T_s$ via non-radiative pathways, however, remains largely unknown.

This study attempts to address these questions by using a modeling framework that focuses on the modification of the terrestrial surface energy budget by aerosols. We first quantify the perturbations to each component of the surface energy budget using a modeling system consisting of an atmosphere model and a global land model. The atmosphere model is run with radiation diagnostics to determine the incoming shortwave and longwave radiation fields at the surface with realistic atmospheric aerosol distributions and in a hypothetical atmosphere with aerosols removed but with clouds intact. The remaining components of the surface energy budget are simulated by forcing the land model with the two sets of atmosphere results. In the two simulations, the incoming shortwave (beam and diffuse) and incoming longwave radiation are different, but other forcing variables (air temperature, humidity and wind) at the first grid height and surface variables (precipitation and air pressure) remain the same. A comprehensive evaluation of the simulation results at the appropriate scales using multiple data sources confirms that the modeling setup captures the general direction of these interactions. In parallel, using an offline decomposition analysis of the surface energy budget, we quantify the contributions of aerosol radiative and non-radiative pathways to local surface temperature perturbations ($\Delta T$). Since the non-radiative pathways are expected to be strongly mediated by the biophysical characteristics of the surface (Bonan, 2008), we quantify the relative strength of these pathways across different climate and vegetation density zones. Finally, using a third land model run and offline calculations, we isolate the contributions of the aerosol global dimming effect and the diffuse radiation fertilization effect on EF, the carbon budget, and $T_s$. We find that the aerosol-induced $\Delta T$ through the non-radiative pathways is large, especially over vegetated surfaces.

## 2. Materials and Methods

### 2.1. Modeling Framework to Isolate the Impact of Aerosols on the Surface Energy Budget

The Earth's surface energy budget represents the thermodynamic interactions between the surface and the adjacent air layer and is expressed as

$$K_\downarrow + L_\downarrow - K_\uparrow - L_\uparrow = H + \lambda E + G, \tag{1}$$

where $K_\downarrow$ is the incoming shortwave radiation, $L_\downarrow$ is the incoming longwave radiation, $K_\uparrow$ is the shortwave radiation reflected by the surface, $L_\uparrow$ is the longwave radiation emitted by the surface, $H$ is the sensible heat flux and represents the turbulent transfer of heat from the surface to the atmosphere, $\lambda E$ is the latent heat flux or the transfer of moisture from the surface to the atmosphere, and $G$ is the ground flux. The terms on the left-hand side of Equation 1 comprise the surface net radiation,

$$R_n = K_\downarrow + L_\downarrow - K_\uparrow - L_\uparrow, \tag{2}$$

We use the Community Atmosphere Model (CAM, version 6.0 with slab ocean, prescribed sea ice and present-day climatological distribution of aerosols; Gettelman et al., 2019) and the Community Land Model (CLM, version 5.0 with biogeochemistry and prognostic vegetation state turned on; Lawrence et al., 2019) to quantify the impact of aerosols on each component of Equation 1 for the period 2001–2003. We run these models twice at a resolution of $0.9375 \times 1.5°$. The first run, labeled as $P$, is for the polluted atmosphere. Atmospheric forcing variables produced by CAM at the screen height and at the surface (incoming solar radiation, incoming longwave radiation, air temperature, specific humidity, wind speed, atmospheric pressure, precipitation) are used as inputs to drive CLM. By default, CLM in land-only mode partitions $K_\downarrow$ into the diffuse ($K_{\downarrow,d}$) and the beam ($K_{\downarrow,b}$) component using a polynomial fit function of $K_\downarrow$. In the present study, we bypass this default partitioning, and instead use $K_{\downarrow,d}$ and $K_{\downarrow,b}$ calculated by CAM. The use of prescribed $K_{\downarrow,d}$ and $K_{\downarrow,b}$ in CLM instead of its default partitioning scheme has been shown to better capture both the magnitude of gross primary productivity (GPP) and the GPP response to diffuse fraction $k_d$ ($=K_{\downarrow,d}/K_\downarrow$) for a temperate deciduous forest site (Wozniak et al., 2020). To allow the land processes to adjust to the different forcing sets, the same three years of forcing are looped six times. The results from the final three-year loop are presented. The relatively short time period used is justified since this is a study of perturbation and not change over time. Short periods are also used in other perturbation studies (Matsui et al., 2008; Rap et al., 2018).

In the second run (labeled as $C$), the incoming solar and incoming longwave radiation are calculated with the diagnostic radiation transfer code of CAM but without aerosols. All other CLM forcing variables (air temperature, specific humidity, wind speed, atmospheric pressure, precipitation) are identical to those in Run P. The results are for a hypothetical atmosphere free of aerosols.

The effect of aerosols on the surface radiation and energy processes is quantified as the difference between Run $P$ and Run $C$. For example, $K_{\downarrow,d}$ is 62.88 W m$^{-2}$ in the polluted atmosphere in Run $P$ and 52.09 W m$^{-2}$ in the clean atmosphere in Run $C$, giving $\Delta K_{\downarrow,d}$ of 10.79 W m$^{-2}$. $K_{\downarrow,d}$ is greater in $P$ than in $C$ because the former includes contributions from scattering by aerosols, gaseous molecules, and clouds whereas the latter include only contributions from scattering by gaseous molecules and clouds. The interaction of aerosols with clouds is simulated by default in CAM and does not affect the diagnostic radiation calculation. Thus, in Run $C$, the clouds from Run $P$ are preserved. Had all aerosols been removed from the atmosphere in the default CAM setup, practically all clouds would have disappeared. We perform a third run, labeled as $M$, to help separate the global dimming and diffuse radiation fertilization effects. In this simulation, $K_\downarrow$ is the same as in the polluted run ($P$) and $k_d$ is kept the same as in the clean run (C). The overall change in a variable $X$ due to aerosols can then be decomposed as

$$\Delta X = \left( X_P - X_M \right) + \left( X_M - X_C \right), \tag{3}$$

where subscript $M$, $P$, and $C$ denote the three simulations, ($X_P$ - $X_M$) represents the contribution arising from change in radiation quality or the diffuse radiation fertilization effect, and ($X_M$ - $X_C$) represents the contribution arising from change in radiation quantity or the dimming effect. The global (and regional; see next
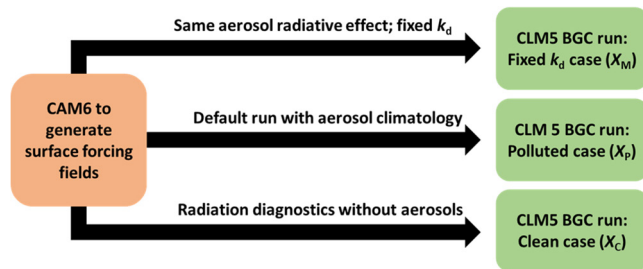
**Figure 1.** Schematic of modeling setup used in the present study. The forcing fields from CAM6 include incoming diffuse radiation, incoming direct beam radiation, incoming longwave radiation, air temperature, specific humidity, wind speed, atmospheric pressure, and precipitation. Only the diffuse radiation, direct beam radiation, and longwave radiation are changed in the different runs to represent the impact of aerosols on the components of the incident radiation at the surface.

subsection) means, as well as their standard deviations or standard errors (as noted in the corresponding text or figure and table captions), are calculated after weighing the gridded values by the grid areas. A schematic of the modeling setup is in Figure 1.

## 2.2. Model Evaluation

The realism of the CAM and CLM results (Table S1) are assessed by comparison with multiple independent data products. The CLM forcing data simulated by CAM are compared with the Global Soil Wetness Project version 3 (GSWP3) data set (Dirmeyer et al., 2011), the standard atmospheric forcing data used in the Land Model Intercomparison Project (LUMIP) (Lawrence et al., 2016). The components of the surface energy budget from the model runs are also evaluated using NASA's MERRA-2 reanalysis (Gelaro et al., 2017), while the simulated sensible and latent heat fluxes are further evaluated against the FLUXCOM data set, which merges FLUXNET observations with remote sensing phenology and meteorological data (Jung et al., 2019). We choose the ensemble FLUXCOM estimates from all the machine learning models based on the GSWP3 meteorological forcing for this purpose. We also use observations from the Global Energy Balance Archive (GEBA) (Wild et al., 2017) to evaluate grid-level incoming shortwave and diffuse radiation. Perturbations to the surface radiation budget due to aerosols are compared against the MERRA-2 radiation diagnostics and two previous global studies. The statistical parameters used for model evaluation are the coefficient of determination ($r^2$), the root-mean-square error (RMSE), and the mean bias error (MBE). For comparisons against the gridded datasets, the same time-period as the model run (2001–2003) is used for all terrestrial surfaces as well as for each individual Koppen-Geiger climate class, namely tropical, arid, temperate, boreal, and polar (Rubel & Kottek, 2010; Figure S1a). For GEBA observations, only the years for which all 12 months of data are available are selected. Since the CAM-CLM run represents the climatological mean of the radiation fields, GEBA sites with at least 3 years of data are averaged to create monthly composites. To check how well the aerosol optical depth (AOD) in CAM and leaf area index (LAI) in CLM, two important parameters that modulate aerosol-biosphere-climate interactions, compare to observations, we use 5-years averages (2003–2007) derived from the Moderate Resolution Imaging Spectroradiometer (MODIS) observations (Knyazikhin et al., 1998; Lyapustin et al., 2018) for each climate zone.

Table S2 shows the evaluation of the forcing fields. We see relatively low $r^2$ values for almost all the variables for the tropical region. This is probably due to the difference in cloud distribution associated with different parameterizations used in the models. However, overall, our mean forcing fields are comparable to the GSWP3 data, except for wind speed (RMSE = 2.39 m s$^{-1}$), though that should not affect our perturbation runs much. Moreover, our overall results are presented at the areally averaged climate zone scale, not for individual grid values.

We evaluate the gridded incoming diffuse radiation and total shortwave radiation against observations, both globally and for each climate zone, and find the results to be reasonable (MBE = 10.20 W m$^{-2}$ for shortwave; −10.52 W m$^{-2}$ for diffuse for all sites; Figures S2 and S3). Note that the underestimation of $k_d$ due to the overestimation of shortwave radiation and underestimation of diffuse radiation will introduce some uncertainties in the magnitude of our results. This underestimation may be due to the lower AOD in CAM compared to MODIS MCD19A2 version 6 observations (Lyapustin et al., 2018), seen for all climate zones except the arid zone (Figure S4b), which is consistent with the results from a recent study (Y. Wang et al., 2021). The evaluation for longwave radiation is not shown since there are very few stations with at least three years of incoming longwave observations in GEBA. The slight difference in incoming shortwave and longwave radiation between Tables S3, S1 and Table S2 is because they are re-gridded from datasets at different resolution. The MERRA-2 reanalysis assimilates satellite-based observations of aerosols and uses them to isolate the direct radiative effect of aerosols (Gelaro et al., 2017). The magnitude of the shortwave and longwave aerosol radiative effects from our CAM run are very similar to the MERRA-2 diagnostics

**Table 1**

*Comparison of Change to the Surface Energy Budget Terms Due to Aerosols With MERRA-2 Data and Chen and Zhuang (for Radiation components) and Liu et al. (for Turbulent Fluxes). The Units are in W $m^{-2}$*

| Variable | Case | Source | | |
|---|---|---|---|---|
| | | Liu et al.; Chen and Zhuang | Present study | MERRA-2 |
| Sensible heat flux | Without aerosols | 95.26 | $35.64 \pm 29.7$ | NA |
| | With aerosols | 79.57 | $32.05 \pm 27.86$ | $35.37 \pm 33.06$ |
| | Change | $-15.69$ | $-3.59 \pm 3.03$ | NA |
| Latent heat flux | Without aerosols | 46.00 | $37.93 \pm 29.68$ | NA |
| | With aerosols | 43.60 | $37.42 \pm 29.23$ | $43.13 \pm 37.3$ |
| | Change | $-2.4$ | $-0.51 \pm 0.8$ | NA |
| Change in incoming shortwave | | $-21.9$ | $-8.72 \pm 8.98$ | $-8.49 \pm 6.82$ |
| Change incoming longwave | | NA | $2.12 \pm 3.73$ (all-sky) | $1.02 \pm 1.54$ (clear-sky) |

(Table 1). Note that MERRA-2 only provides clear-sky $\Delta L_\downarrow$ due to aerosols, which contributes to larger relative deviations from CAM ($2.12 \pm 3.73$ W $m^{-2}$ for CAM vs. $1.02 \pm 1.54$ W $m^{-2}$ in MERRA-2).

Table S3 shows comparison of the simulated surface energy budget components against the MERRA-2 reanalysis dataset. In addition to the expected low explanation of variability in the tropical region, there is a large difference in the magnitude and variability of $G$ between MERRA-2 and CLM ($r^2 = 0.14$; RMSE $= 1.53$ W $m^{-2}$).

Table 2 shows that the latent heat flux simulated by CLM is in excellent agreement with the FLUXCOM data set on both the global scale and for individual climate zones with MBE less than 10%. The agreement for sensible heat flux is also very good except for the boreal and polar climate zones, where CLM shows systematic low biases. The LAI in CLM is slightly higher than the MODIS MCD15A3H version 6 5-years estimates (Figure S4a; Knyazikhin et al., 1998), but the variability between the climate zones is generally captured by the model.

We also compare our results with those reported by Liu et al. (2014), which appears to be the only other global study on aerosol impact on turbulent fluxes on land (Table 1). Our reductions in $H$ and $\lambda E$ are lower than theirs (Table 1). While Liu et al. (2014) did not provide the results for $\Delta K_\downarrow$, Chen and Zhuang (2014),

**Table 2**

*Evaluation of the Sensible and Latent Heat Fluxes Simulate by CLM Against FLUXCOM Data for the World's Land Surfaces and for Each Climate Zone*

| Variable | Case | Regions of interest | | | | | |
|---|---|---|---|---|---|---|---|
| | | Global land | Tropical | Arid | Temperate | Boreal | Polar |
| Sensible heat flux (W $m^{-2}$) | CLM | $37.42 \pm 20.54$ | $41.77 \pm 14.21$ | $57.17 \pm 14.95$ | $40.78 \pm 14.53$ | $19.88 \pm 12.27$ | $18.78 \pm 23.07$ |
| | FLUXCOM | $40.87 \pm 15.82$ | $44.06 \pm 10.47$ | $56.51 \pm 12.89$ | $39.09 \pm 14.34$ | $28.71 \pm 8.01$ | $32.1 \pm 19.24$ |
| | $r^2$ | 0.71 | 0.32 | 0.47 | 0.48 | 0.44 | 0.81 |
| | RMSE | 12.40 | 11.99 | 11.55 | 11.88 | 12.94 | 16.11 |
| | MBE | $-3.45$ | $-2.29$ | 0.67 | 1.69 | $-8.83$ | $-13.31$ |
| Latent heat flux (W $m^{-2}$) | CLM | $45.23 \pm 26.29$ | $79.81 \pm 17$ | $32.12 \pm 15.61$ | $51.7 \pm 16.74$ | $27.84 \pm 10.55$ | $19.2 \pm 13.64$ |
| | FLUXCOM | $48.38 \pm 27.49$ | $86.32 \pm 18.29$ | $32.3 \pm 11.8$ | $56.34 \pm 15.05$ | $30.03 \pm 8.95$ | $20.29 \pm 9.75$ |
| | $r^2$ | 0.87 | 0.52 | 0.42 | 0.66 | 0.73 | 0.62 |
| | RMSE | 10.98 | 14.54 | 11.92 | 10.97 | 6.36 | 8.11 |
| | MBE | $-3.14$ | $-6.51$ | $-0.18$ | $-4.64$ | $-2.20$ | $-1.09$ |

*Note.* The top two rows for each variable show the grid-area weighted mean and standard deviation from the present study and FLUXCOM. The statistical parameters for model evaluation are the coefficient of determination ($r^2$), the weighted root-mean-square error (RMSE), and the mean bias error (MBE). CLM, Community Land Model.

who used the same modeling framework, reported a $\Delta K_{\downarrow}$ of $-21.9$ W m$^{-2}$ (global terrestrial mean) due to aerosols, which is higher in magnitude than previous studies (Chung et al., 2005; scaled by AOD over land), as well as MERRA-2 (Table 1). Moreover, as also mentioned by the authors, the magnitude of $H$ simulated by their model is significantly higher than other estimates. Since our $\Delta K_{\downarrow}$ is in good agreement with the MERRA-2 diagnostics and our simulated sensible and latent heat fluxes are much closer to FLUXCOM and MERRA-2 estimates than theirs (Tables 1 and 2), we are relatively confident about the overall magnitude of the changes in turbulent fluxes in our study.

Davin and Seneviratne (2012) used an older version of CLM (CLM3.5; see changes since then in Oleson et al., 2013 and Lawrence et al., 2019) with a two-big-leaf canopy structure to demonstrate that it can simulate the enhancement of $\lambda E$ under diffuse light conditions as observed at an evergreen needleleaf forest site. However, a recent study using the multi-layer implementation of CLM at a temperate deciduous forest site suggests an overestimation of the GPP response to $k_d$ at the hourly scale during summer (Wozniak et al., 2020). Our results are less prone to this model uncertainty because the temperature change induced by the fertilization effect is minor in comparison to the change associate with Bowen ratio increase under reduced global radiation which is a robust feature across models (Davin & Seneviratne, 2012; Liu et al., 2014; Matsui et al., 2008; Mercado et al., 2009; Oliveira et al., 2011; Rap et al., 2018, 2015; Zhang et al., 2008) and in observational studies (Kanniah et al., 2012; K. Wang et al., 2008; S. Wang et al., 2018; W. Wang et al., 2018).

### 2.3. Terrestrial Evapotranspiration and Its Partitioning

The terrestrial evapotranspiration can be separated into evaporation from the ground ($\lambda E_g$), evaporation from the canopy ($\lambda E_c$), transpiration ($\lambda E_t$) from sunlit leaves ($\lambda E_{t,\text{sun}}$), and transpiration from shaded leaves ($\lambda E_{t,\text{sha}}$). This separation in CLM is based on the vegetation temperature, ground temperature, surface temperature, and specific humidity. The method starts with initial guesses for wind speed and Monin-Obukhov length, which are used to iteratively solve for the other components and sub-components of the surface energy budget. More information about this numerical scheme can be found in Oleson et al. (2013).

Of specific importance to the present study, CLM parameterizes photosynthesis and transpiration separately for sunlit and shaded leaves, but it represents the whole canopy with a single foliage temperature (Dai et al., 2004). To determine if this simplification adversely affects our perturbation experiments, we compared the CLM results with the results of the Community Atmosphere-Biosphere Land Exchange model (CABLE version 1.4: Kowalczyk et al., 2006). Unlike CLM, CABLE solves the energy balance equation and the foliage temperature separately for sunlit and shaded leaves (Wang & Leuning, 1998). The comparison was made for three grid cells where >90% of the grid space is occupied by a single plant functional type (PFT). Two of the grids are occupied by broadleaf evergreen trees, one with the highest ($-22.3$ W m$^{-2}$; labeled as BET1, in Congo Basin; 3.3°N, 17.5°E) and the other with the lowest ($-1.5$ W m$^{-2}$; labeled as BET2, in Papua New Guinea; 3.3°S, 137.5°E) magnitude of the aerosol shortwave radiative effect $\Delta K_{\downarrow}$, both with a LAI of about 6. The third grid is C3 grass with LAI of 2.1 and $\Delta K_{\downarrow}$ of $-6.6$ W m$^{-2}$ (labeled as C3, in northern China; 49.5°N, 118.7°E).

For each grid cell, CABLE was prescribed with the corresponding PFT. The default LAI assigned to the relevant PFTs in CABLE was replaced by the monthly LAI calculated by CLM. The CABLE simulations were forced by the same atmospheric variables as in the CLM runs under clean and polluted conditions. To do this, the CABLE model code was modified to use time-dependent beam fraction of radiation from the CAM simulations. Figure 2 shows the sensible ($H$) and latent heat flux ($\lambda E$), including their components, simulated by the two models for clean sky conditions and their changes due to aerosols, as well as the surface temperature response. The CABLE model confirms that aerosols decrease the Bowen ratio and the surface temperature, by amounts similar to those simulated by CLM. The CABLE simulations also demonstrate broadly similar changes in the sunlit and shaded components of transpiration due to aerosols compared to the CLM simulations.
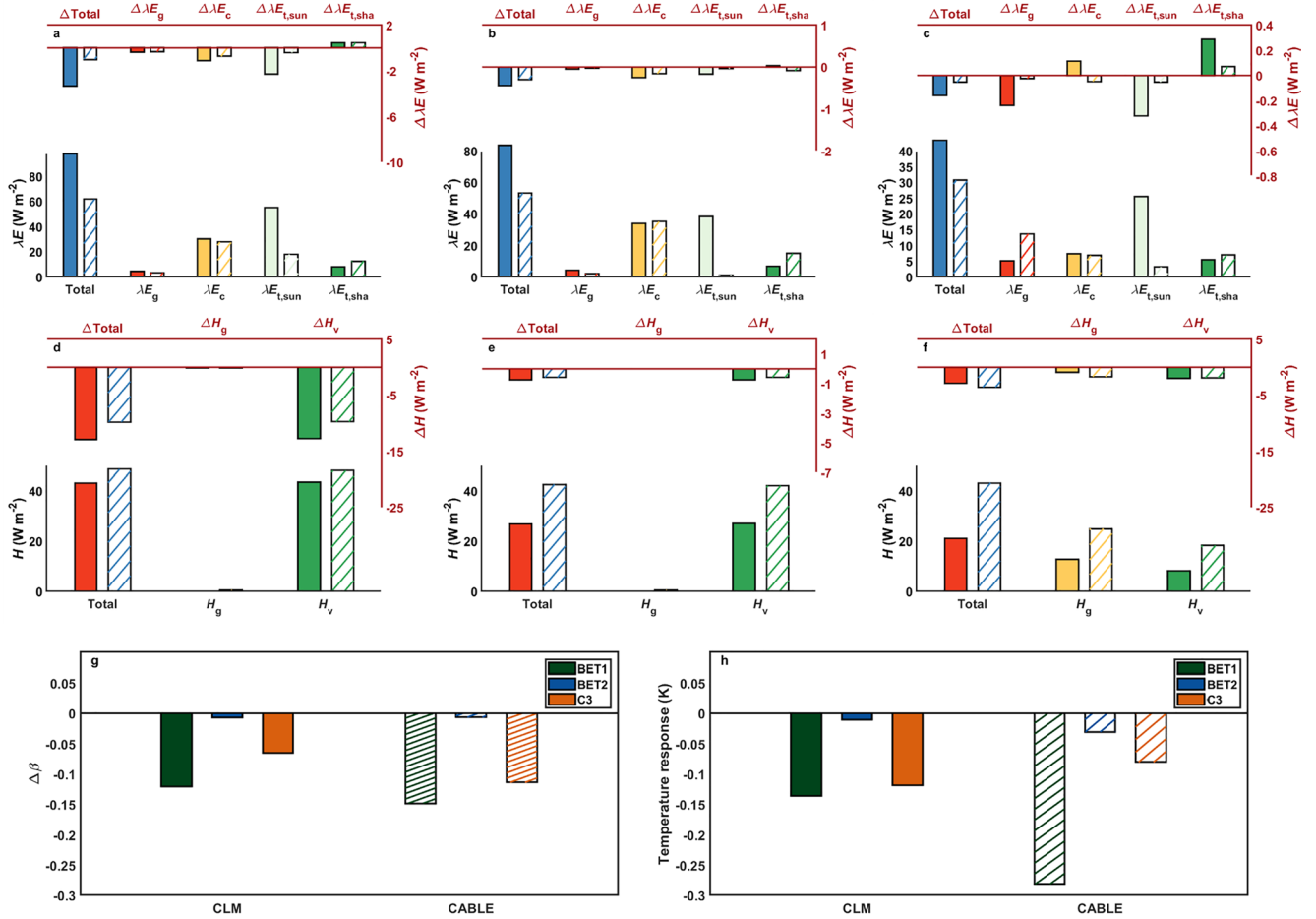
**Figure 2.** Comparisons between CLM and CABLE results. Simulated three-year mean latent heat flux and sensible heat flux, their perturbations, and components for a heavily polluted broadleaf evergreen tree grid (BET1, panels a & d), a lightly polluted broadleaf evergreen tree grid (BET2, panels b & e), and a C3 grass grid (C3, panels c & f). The components for the clean atmosphere are represented by the bars in the lower part of each panel, and the net changes due to aerosols are given by the bars in the upper part. Panel g shows the Bowen ratio response to aerosols. Panel h shows the surface temperature response to aerosols. CLM is represented by filled bars and CABLE by hatched bars. CABLE, Community Atmosphere-Biosphere Land Exchange model; CLM, Community Land Model.

### 2.4. Attributing Surface Temperature Perturbations Through Radiative and Non-Radiative Pathways

The total surface temperature change ($\Delta T_s$) due to aerosols is the sum of the changes in the blending height temperature ($\Delta T_b$) and the local temperature response ($\Delta T$; Chakraborty & Lee, 2019):

$$\Delta T_s = \Delta T + \Delta T_b . \tag{4}$$

Here, $\Delta T$ arises from the radiative pathway associated with changes in $K_\downarrow$ and $L_\downarrow$ and the non-radiative pathway associated with changes in evaporation and in efficiency of convection between the surface and the lower atmosphere. This temperature response can be decomposed according to the theory of intrinsic biophysical mechanism (IBPM) which is a solution of the perturbed form of Equation 1 (Lee et al., 2011),

$$\Delta T = \frac{\lambda_0}{1+f}\Delta K_\downarrow\left(1-a\right) + \frac{\lambda_0}{1+f}\Delta L_\downarrow + \frac{-\lambda_0}{\left(1+f\right)^2}\left(R_n^* - G\right)\Delta f_1 + \frac{-\lambda_0}{\left(1+f\right)^2}\left(R_n^* - G\right)\Delta f_2 + \frac{\lambda_0}{1+f}\Delta G, \tag{5}$$

where $a$ is the surface albedo, $R_n^*$ is apparent net radiation given by

$$R_n^* = K_\downarrow\left(1-a\right) + L_\downarrow - \sigma T_b^4 . \tag{6}$$

$\sigma$ is the Stefan-Boltzmann constant, $\lambda_0$ is the local temperature sensitivity due to longwave radiative feedback given by:

$$\lambda_0 = \frac{1}{4\sigma T_s^3}, \tag{7}$$

and $f$ is a dimensionless energy redistribution factor, a measure of the efficiency of energy dissipation from the surface to the lower atmosphere through convection and evaporation (Lee et al., 2011). A larger $f$ corresponds to a lower effective local climate sensitivity ($\lambda^*$) according to the relation $\lambda^* = \lambda_0/(1 + f)$.

The IBPM method is a diagnostic tool grounded on a first principle (the surface energy conservation). It separates the surface temperature perturbation into contributions of different biophysical pathways. Accordingly, the terms on the right-hand side of Equation 5 represent, from left to right, the temperature response due to change in incoming shortwave radiation $\Delta K_\downarrow$ (term 1), change in incoming longwave radiation $\Delta L_\downarrow$ (term 2), change in energy redistribution through evaporation (term 3), change in energy redistribution through convection (term 4), and change in ground heat flux $\Delta G$ (term 5). The contribution of the radiative pathway is given by the first two terms, and that of the non-radiative pathway is given by the last three terms. The realism of the IBPM framework has been extensively documented in the past, for example, in studies of temperature perturbation due to urbanization (Zhao et al., 2014), deforestation (Bright et al., 2017; Burokowski et al., 2018), and agricultural activities (Chakraborty et al., 2021; Ruehr et al., 2020), and in a study of lake surface temperature change (S. Wang et al., 2018; W. Wang et al., 2018).

In this diagnostic calculation, the change terms $\Delta K_\downarrow$, $\Delta L_\downarrow$ and $\Delta G$ are given as the difference between the two model runs (P minus C), $R_n^*$ and $\lambda_0$ are based on the values of $K_\downarrow$, $L_\downarrow$, $a$, $T_s$, and $T_b$ for the clean atmosphere, with $T_b$ being the atmospheric temperature at the first CAM model grid height (average 60 m above the surface). The energy redistribution factor (Lee et al., 2011) is calculated from the following diagnostic equation

$$f = \frac{\lambda_0}{T_s - T_b}\left(R_n^* - G\right) - 1. \tag{8}$$

Only grids with a positive value of $f$ are considered. Contributions due to evaporation ($\Delta f_1$) and convection ($\Delta f_2$) are calculated from

$$\Delta f_1 = -f\frac{\Delta\beta}{\beta\left(1 + \beta\right)}, \tag{9}$$

$$\Delta f_2 = -f\frac{\Delta r_a}{r_a}, \tag{10}$$

where $\beta$ and $r_a$ are the average Bowen ratio, the ratio of the sensible and latent heat fluxes, and aerodynamic resistance, respectively, from Runs $P$ (or $M$) and $C$, while the $\Delta$ terms are the changes in the respective variables between the two runs. The role of the EF change is expressed through the $\beta$ change, noting that a negative $\Delta\beta$ corresponds to a positive $\Delta$EF and vice versa. Changes in $\beta$ are very small (close to zero) for boreal and polar climate, leading to unreasonably high values of the third term in Equation 5. The $\Delta T$ through the evaporative pathway is thus set to zero for these grids.

## 3. Results

### 3.1. Aerosol Impact on the Surface Energy Budget

Unsurprisingly, aerosols decrease the incoming surface shortwave radiation and increase the incoming longwave radiation (Figure 3), whose spatial variations are consistent with the geographic distribution of aerosols (Figures S5 and S6). The highest changes in incoming radiation are seen over arid regions like the Sahara Desert and the Middle East, and moderately large changes over heavily polluted regions like
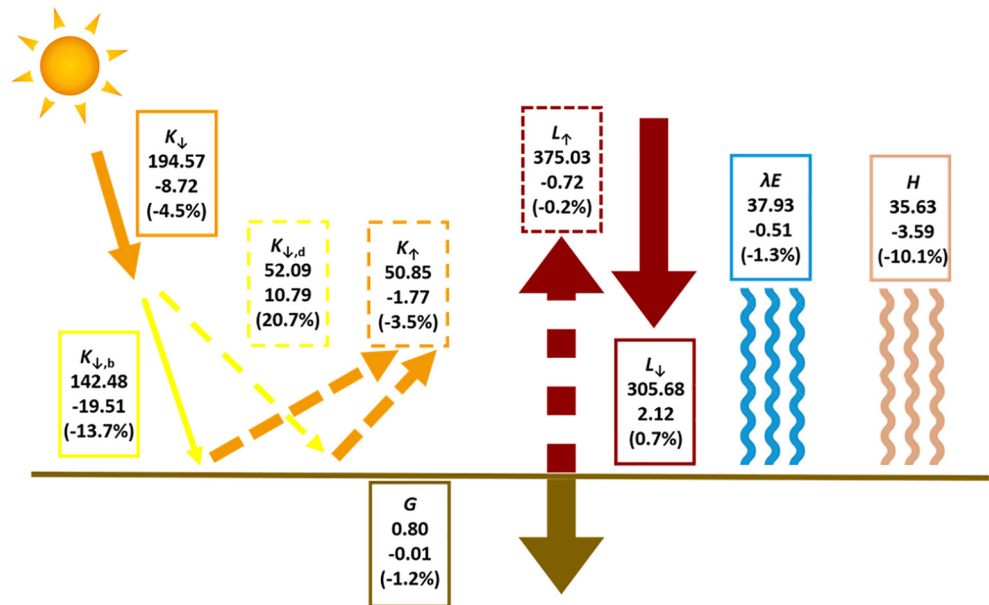
**Figure 3.** Surface energy budget adjustment due to aerosols. Schematic showing grid area-weighted annual mean terrestrial surface energy budget components for a clean atmosphere, namely incoming shortwave radiation ($K_{\downarrow}$), direct beam radiation ($K_{\downarrow,b}$), diffuse radiation ($K_{\downarrow,d}$), reflected shortwave radiation ($K_{\uparrow}$), ground heat flux ($g$), emitted longwave radiation ($L_{\uparrow}$), incoming longwave radiation ($L_{\downarrow}$), latent heat flux ($\lambda E$), and sensible heat flux ($h$), along with changes (and percentage changes) to each component due to aerosols. In each box, the baseline value is at the top, the change is in the middle and the percentage change is in parentheses at the bottom. All quantities other than the percentage changes are in W m$^{-2}$.

northern India and eastern China (Figure S5). The global average reduction in the shortwave radiation $\Delta K_{\downarrow}$ over land is $-8.72$ W m$^{-2}$ ($-4.5\%$), from a base $K_{\downarrow}$ value of 194.57 W m$^{-2}$ for the clean atmospheric state (Figure 3 and Table S1). This total $\Delta K_{\downarrow}$ consists of an increase in the diffuse radiation ($\Delta K_{\downarrow,d}$) by 10.79 W m$^{-2}$ ($20.7\%$) and a decrease in the beam radiation ($\Delta K_{\downarrow,b}$) by 19.51 W m$^{-2}$ ($-13.7\%$). Consequently, the diffuse fraction ($k_d$) increases by 26%, from 0.268 to 0.338. Because of the large mineral dust aerosol loading and of the low base $k_d$ (0.165) due to low cloud amounts and low zenith angle, the largest percentage increase in $k_d$ ($\sim 70\%$) is seen for arid regions. Averaged over all land surfaces, increases in $L_{\downarrow}$ are roughly one-fourth of the decreases in $K_{\downarrow}$, at 2.12 W m$^{-2}$ ($0.7\%$), almost all of which are attributable to natural absorbing aerosols (Chakraborty & Lee, 2019).

Aerosols reduce both the terrestrial sensible ($H$) and the latent heat flux ($\lambda E$), but by different amounts (Figure S7). $H$ decreases over seven times as much as $\lambda E$ ($\Delta H = -3.59$ W m$^{-2}$, $\Delta \lambda E = -0.51$ W m$^{-2}$; Figure 3 and Table S1). Separating $\lambda E$ into its components (Figure 4) explains why $\Delta \lambda E$ is smaller than $\Delta H$ in magnitude. While $\lambda E_g$, $\lambda E_c$, and $\lambda E_t$ decrease, the total decrease in $\lambda E_t$ is partly offset by an increase in $\lambda E_{t,\text{sha}}$. Moreover, the percentage increases in $\lambda E_{t,\text{sha}}$ are much higher than the percentage decreases in $\lambda E_{t,\text{sun}}$. For instance, for the tropical zone (Figure 4b), the increase in $\lambda E_{t,\text{sha}}$ is 8.2%, while the decrease in $\lambda E_{t,\text{sun}}$ is only 2.4%. In this case, $\lambda E_{t,\text{sha}}$ increases by 0.55 W m$^{-2}$, partly offsetting the decrease in $\lambda E_t$ due to $\Delta \lambda E_{t,\text{sun}}$ ($-0.83$ W m$^{-2}$). Similar enhancement of $\lambda E_{t,\text{sha}}$ is also seen for other biomes.

According to the hypothesis of diffuse radiation fertilization, efficient penetration of diffuse radiation through the canopy increases photosynthesis in shaded leaves under polluted conditions. Consequently, this enhances transpiration from shaded leaves and compensates for the lower transpiration from sunlit leaves under the decreased incoming sunlight ($K_{\downarrow}$) due to aerosols. Similar patterns are seen for the components of the ecosystem carbon budget (Figure 5). The net ecosystem productivity (NEP) increases under aerosol loading in most climate zones, with an average increase of 1.7% for the Earth's land surfaces. A similar analysis done for different LAI bins shows that the greatest increase in NEP (and second highest percentage increase) is for grids with LAI > 5 at 0.46 Pg C y$^{-1}$ (Figure S8). The overall change in GPP is positive as opposed to a negative $\Delta \lambda E$, supporting previous finding that aerosol loading enhances ecosystem
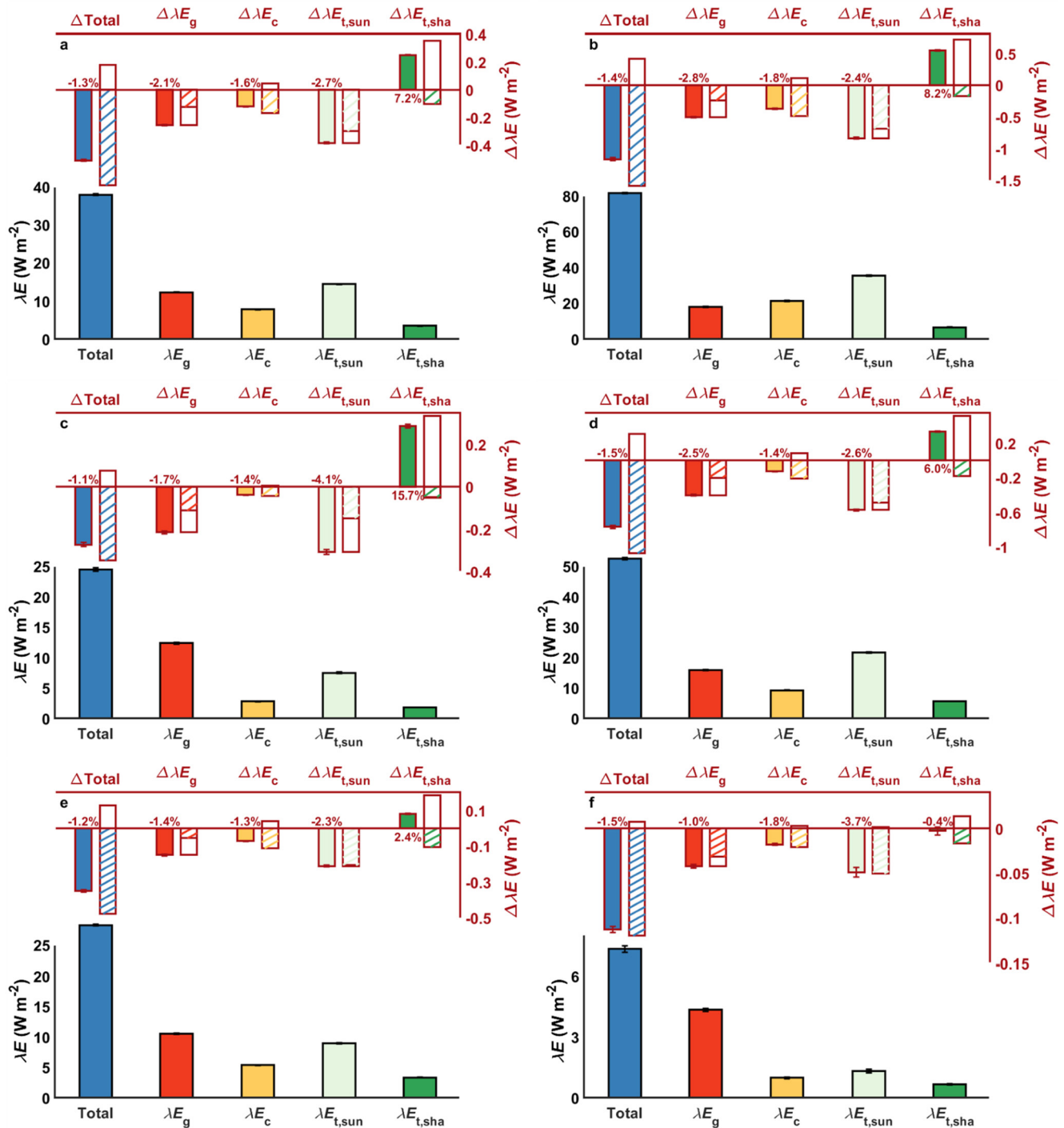
**Figure 4.** Components of latent heat flux and their changes across climate zones. Total grid-area weighted mean latent heat flux ($\lambda E$) for a clean atmosphere and its change due to aerosols ($\Delta\lambda E$), as well as the corresponding components, namely ground evaporation ($\lambda E_g$), canopy evaporation ($\lambda E_c$), transpiration from sunlit leaves ($\lambda E_{t,\text{sun}}$), and transpiration from shaded leaves ($\lambda E_{t,\text{sha}}$) over (a) all terrestrial surfaces, (b) tropical climate, (c) arid climate, (d) temperate climate, (e) boreal climate, and (f) polar climate. The components for a clean atmosphere are represented by the filled bars in the lower part of each panel. The net changes in the components due to aerosols are given by the filled bars in the upper part of the panel, with the percentage change noted. The net change is further decomposed into contributions from the diffuse radiation fertilization effect (blank) and the dimming effect (hatched). The error bars represent the grid area-weighted standard errors.
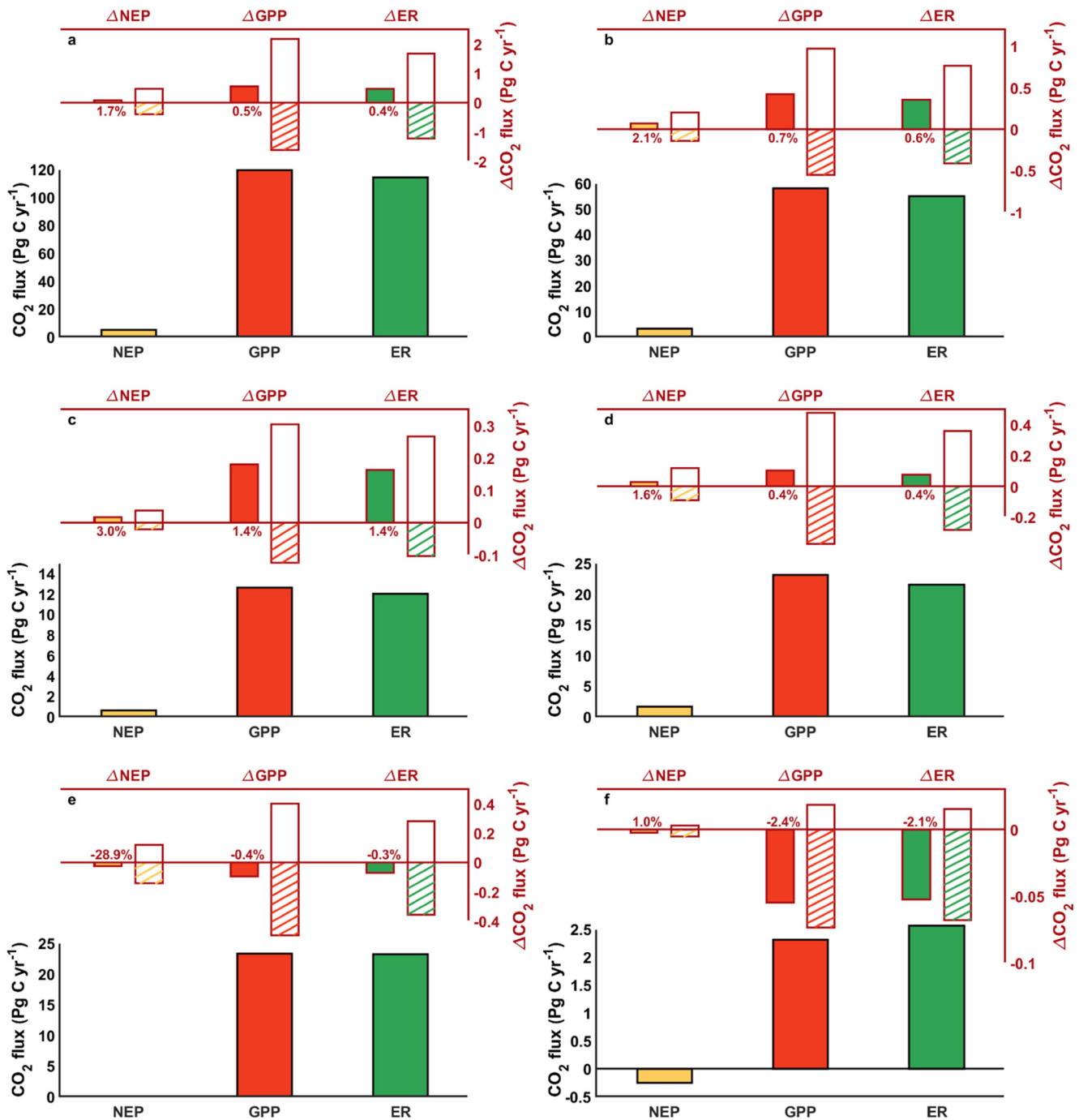
**Figure 5.** Carbon budget across climate zones. Net ecosystem production (NEP, orange bar), gross primary productivity (GPP, red bar), and ecosystem respiration (ER, green bar) over (a) All terrestrial surfaces, (b) Tropical climate, (c) Arid climate, (d) temperate climate, (e) Boreal climate, and (f) Polar climate. The carbon flux components for a clean atmosphere are represented by the filled bars in the lower part of each panel. The net changes due to aerosols are given by the filled bars in the upper part of the panel, with the percentage changes noted. The net changes are further decomposed into contributions from the diffuse radiation fertilization effect (blank bar) and the dimming effect (hatched bar).
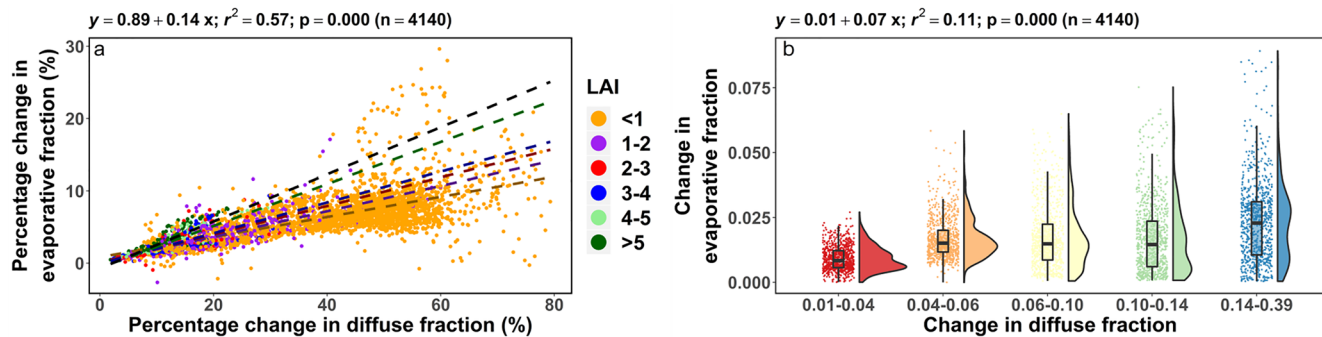
**Figure 6.** Association between diffuse fraction change and evaporative fraction change. (a) Scatter plot of grid-averaged percentage change in diffuse fraction ($k_d$) versus percentage change in evaporative fraction (EF) between polluted and clean atmosphere. The equation for the linear relationship between the two is given above the figure. The dashed lines, from dark orange to black, are the lines of best fit between the two variables for increasing leaf area index (LAI) bins. (b) Association between grid-averaged changes in EF and in diffuse fraction ($\Delta k_d$) between polluted and clean atmosphere. The regression equation between the two is given above the figure, with coefficient of determination $r^2$, confidence level $p$, and number of grid points $n$ noted. For each equal-sized $\Delta k_d$ bin, frequency distributions of $\Delta$EF, as well as box and whisker plots showing the 25th, 50th, and 75th percentile of $\Delta$EF are given.

water use efficiency (Lu et al., 2017). The diffuse radiation fertilization effect alone has a stronger impact on GPP (increase of 2.18 Pg C y$^{-1}$ or 1.8% of total terrestrial GPP, Figure 5a) than on land evaporation (increase of 0.18 W m$^{-2}$ or 0.48% of total terrestrial evaporation, Figure 4a).

For $\Delta H$, there is no corresponding compensating mechanism; instead $H$ from both the ground ($H_g$) and vegetation ($H_v$) decrease (Figure S9). As a result, EF increases by 0.023 or 4.5% over the global terrestrial surface (Figure S7). Changes in EF reach 0.05–0.06 (almost 10%) over the Congo Basin rainforest in central Africa, northern India, and eastern and north-western China. Taklamakan Desert in north-western China shows the highest percentage change in EF (25%–30%).

The percentage changes in EF are positively correlated with percentage changes in $k_d$ and strongly modulated by vegetation density, as seen from the steeper slopes of the linear fit between them for increasing LAI bins (Figure 6a). The sensitivity of percentage change in EF to percentage changes in $k_d$ increases from 0.14 for grids with an LAI less than 1-0.32 for grids with an LAI greater than or equal to 5. Similarly, the actual change in EF shows an increasing trend with increasing $\Delta k_d$, though the correlation between the two is weaker (Figure 6b) than between the relative changes since the base available energy varies widely between different grids.

For this analysis, we used the latest version of CLM with biogeochemistry and prognostic vegetation. To illustrate the validity of our conclusions within the modeling framework, we ran an earlier version of the model (CLM4.5) with the same forcing data and obtained broadly consistent results (Figure S11).

### 3.2. Isolating Multiple Pathways of Aerosol-Induced Local Temperature Response

Using the theory of IBPM (Lee et al., 2011), we separate the contributions of different pathways, namely surface shortwave radiative effect, surface longwave radiative effect, change in EF, change in convection efficiency or aerodynamic resistance, and change in the ground heat flux, to the total surface temperature perturbation ($\Delta T$; Figure 7 and S12). Note that $\Delta T$ only refers to the local temperature response to aerosols. The total aerosol-induced surface temperature change is the sum of this local response and the background atmospheric temperature change (Equation 4). Here, the realism of the IBM method is further supported by the good agreement between the temperature perturbation computed online (gray bars, the "truth") and the perturbation calculated with IBPM (red bars, Figure 7).

The magnitude of $\Delta K_\downarrow$ is higher in regions of higher aerosol loading (Figures S5 and S6). The highest values are seen in the arid regions. Overall, the surface shortwave radiative effect reduces the global terrestrial surface temperature by 0.15 K, while the longwave radiative effect increases it by 0.05 K. The contributions of these radiative pathways are determined by both the radiation changes and the effective local climate sensitivity ($\lambda_*$)—the change in local surface temperature due to a unit surface radiative forcing (Chakraborty
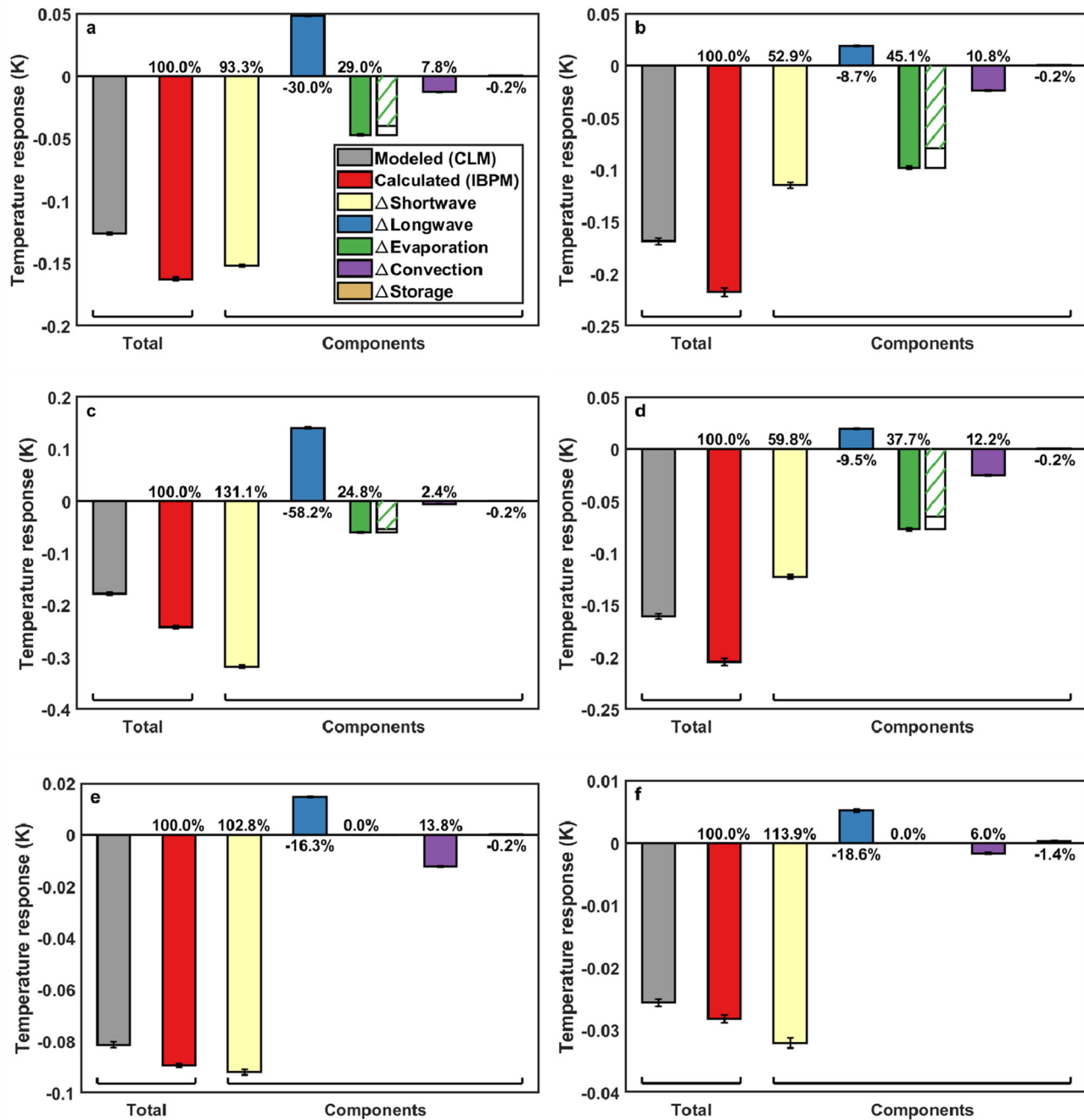
**Figure 7.** Comparing modeled and diagnosed surface temperature response. Total grid-area weighted mean calculated (red, IBPM) and modeled (gray, CLM) temperature response due to aerosols, as well as calculated component contributions from changes in incoming shortwave radiation (light yellow, $\Delta K_\downarrow$), incoming longwave radiation (blue, $\Delta L_\downarrow$), evaporation (green, $\Delta EF$), convection (purple, $\Delta r_a$), and ground heat storage (dark yellow, $\Delta G$) over (a) all terrestrial surfaces, (b) tropical climate, (c) arid climate, (d) temperate climate, (e) boreal climate, and (f) polar climate. The temperature response through evaporation is further decomposed into the contributions from the diffuse radiation fertilization effect (blank bar) and the dimming effect (hatched bar). The percentage value denotes the relative component contribution to the total temperature response. Error bars represent the grid area-weighted standard errors. IBPM, intrinsic biophysical mechanism; CLM, Community Land Model.

& Lee, 2019). The magnitude of $\lambda_*$ is higher for smooth surfaces, such as deserts and snowpack, and lower for rough surfaces, such as forests (Figure S13). Subsequently, the temperature response to the radiative effect are higher in arid regions and lower in the tropical forests (Figure S12). The highest perturbations (<−0.4 K) occur in north-western China, central Australia, and the Middle East, where both the radiation

changes and $\lambda_*$ are high. In comparison, the Amazon rain forest shows low response to the radiative pathways, with decreases of less than 0.1 K (Figure S12a).

In contrast, the highest perturbations through the non-radiative pathways (sum of evaporation and convection) occur in the Congo Basin (up to $-0.6$ K), eastern China (up to $-0.5$ K), and northern India (up to $-0.4$ K). All of these regions have dense vegetation cover and relatively high aerosol loading. The Amazon basin does not show a high response to the non-radiative pathways (less than 0.05 K) since aerosol loading is relatively low over this region (Figures S6 and S12d). Taken together, the non-radiative pathways reduce the annual mean terrestrial surface temperature by about 0.06 K. Although aerosols may change $r_a$ through modification of atmospheric stability (Talukdar et al., 2019), we find that the magnitude of this effect is minor compared to the enhancement of evaporative cooling.

The overall change in the annual mean terrestrial surface temperature $\Delta T$ is $-0.16$ K. The highest $\Delta T$ is seen in the arid zone, followed by the tropical, temperate, boreal, and polar climate zones (Figure 7). The evaporative pathway accounts for $\sim$29% of the total $\Delta T$ globally, and for as much as 45% in the tropical climate zone. To our knowledge, this is the first isolation of the local temperature response to aerosols through the evaporative pathway. Although it is intuitive that increased water loss in plants will lead to surface cooling, what is surprising is the strength of this pathway.

### 3.3. Dependence on Vegetation Density

The evaporative contribution to the total temperature response increases with increasing LAI, though the total temperature response itself decreases (Figure 8a). At an LAI of around 2, the $\Delta T$ via the evaporative pathway exceeds the $\Delta T$ due to the surface radiative effect (Figure 8b). At grids with high LAI ($>2$), the effective local climate sensitivity is much lower (mean $\lambda_*$ of 0.013 K W$^{-1}$ m$^2$ vs. global mean of 0.029 K W$^{-1}$ m$^2$), reducing the surface temperature response through the radiative pathway and thus leading to the relatively large contribution of aerosol-induced evaporation to $\Delta T$. In comparison, arid regions have low LAI (regional mean LAI of 0.39) and high climate sensitivity (regional mean $\lambda_*$ of 0.026 K W$^{-1}$ m$^2$), leading to the low contribution of the evaporative pathway to $\Delta T$ (Figure 7b). Of the three climate zones considered, LAI is greater than 2 in 58% of the tropical grids, 45% of the temperate grids, and 0.6% of the arid grids (Figure S1b). Overall, high percentage contributions of the evaporative pathway to the aerosol-induced local temperature response are seen over the tropical rainforests in both South America and Africa (Figure 8c).

### 3.4. Global Dimming Versus Diffuse Radiation Fertilization

Since aerosols simultaneously reduce $K_\downarrow$ and increase $k_d$, an open question is whether the aerosol-induced changes in EF, GPP, and surface temperature are caused by changes in the quantity or in the quality of solar radiation (Oliveira et al., 2011). To answer this question, we conducted a third numerical experiment to help separate the total change in a variable into contributions from change in radiation quality or the diffuse radiation fertilization effect and from change in radiation quantity or the dimming effect. Overall, the fertilization effect is more important for GPP and NEP than for $\lambda E$, increasing the global mean $\lambda E$ by only 0.18 W m$^{-2}$ or 0.48% (Figure 4a) and global annual NEP by 0.49 Pg C and GPP by 2.18 Pg C (1.8%; Figure 5a). For intensive aerosol emission episodes, such as fires and volcanic eruptions, net reductions in GPP and yield have been demonstrated in previous studies (Proctor et al., 2018; Yue & Unger, 2018). Here, we find that for the sum of all aerosols (natural plus anthropogenic), the fertilization effect is stronger than the dimming effect, resulting in a net increase in GPP, which suggests that most ecosystems are light-saturated, although the change is less than half the total change seen in Chen and Zhuang (2014).

In the case of $\lambda E$, the fertilization effect is much weaker than the dimming effect, resulting in a net reduction in $\lambda E$ (Figure 4). For transpiration, only the shaded canopy shows a positive fertilization effect. That the percentage increase in GPP is higher than the percentage reduction in $\lambda E$ supports the conclusion that diffuse radiation enhances ecosystem water use efficiency (Kanniah et al., 2012; Knohl & Baldocchi, 2008). Dimming dominates the evaporative response to aerosols, contributing 84% to the global EF increase, with the remaining increase (16%) coming from the fertilization effect. Consequently, 84% and 16% of the cooling due to EF change of the terrestrial surface (81% and 19% for tropical areas) are attributed to the dimming and the fertilization effect, respectively (Figure 7). It would not be feasible to obtain the diagnostic insights,
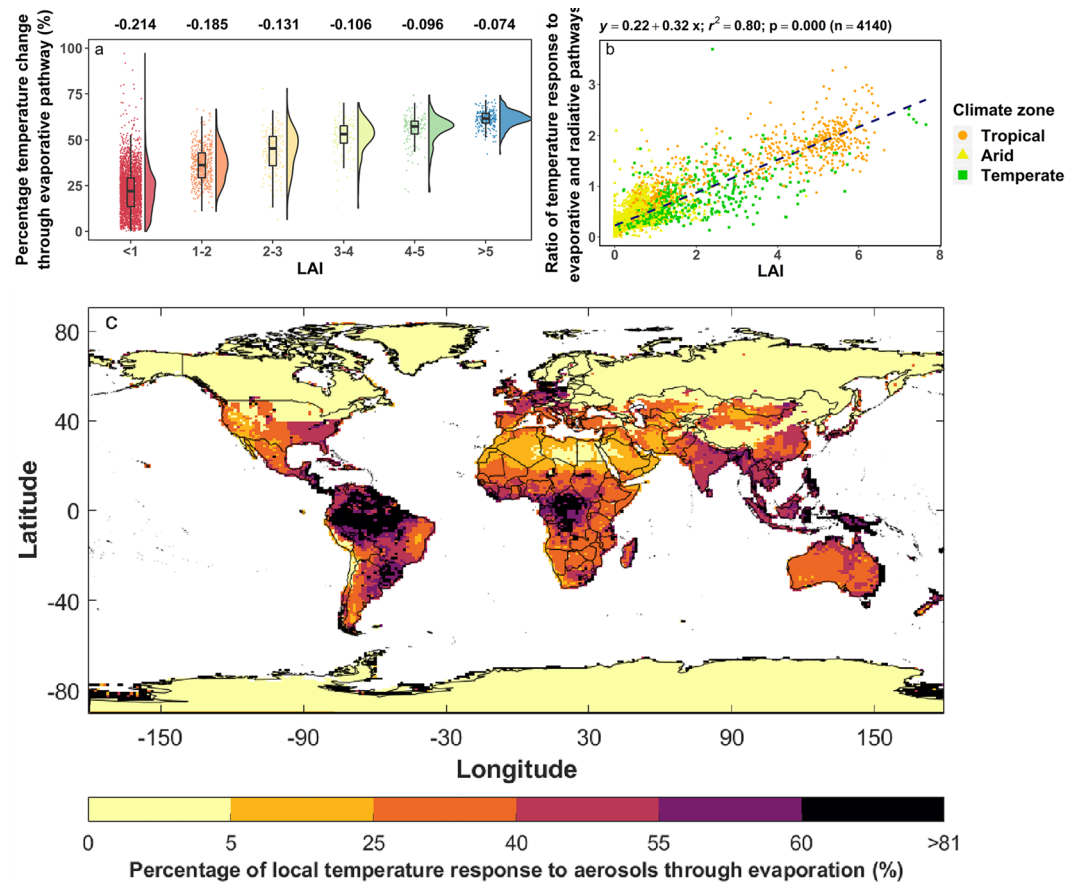
**Figure 8.** Contribution of evaporative pathway to aerosol-induced surface temperature perturbation. (a) Percentage of surface temperature change attributed to the evaporative pathway in increasing leaf area index (LAI) bins. Each data point represents one grid mean value. The box and whisker plot indicates 25th, 50th and 75th percentile values, with the frequency distribution given to the left. The median of the total local surface temperature change in K for each LAI bin is at the top of the figure. (b) Scatter plot of grid-averaged ratio of temperature change attributed to change in evaporation and that attributed to changes in surface shortwave and longwave radiation. The linear regression equation is given above the figure and the dashed line is the line of best fit between the two variables. The three colors represent three climate zones. (c) Global map of percentage contribution of the evaporative pathway to total local temperature response to aerosols.

such as shown in Figure 8b, using only a fully-coupled simulation because of the interactive nature of different biophysical processes. For example, by perturbing $K_\downarrow$ in the coupled simulation, the EF will also change, and we would not know whether the surface temperature change is caused by the change in $K_\downarrow$ or by the change in EF.

## 4. Discussion

The results of our global scale modeling are broadly consistent with those reported in ecosystem (Knohl & Baldocchi, 2008) and regional scale studies (Davin & Seneviratne, 2012; Matsui et al., 2008). The stronger effect of diffuse radiation on canopy photosynthesis for higher LAI values (which we see for EF in Figure 6a) was seen using multi-layer model simulations at a deciduous temperate forest (Knohl & Baldocchi, 2008). Matsui et al. (2008) found that $H$ is reduced more than $\lambda E$ by aerosol pollution over eastern United States ($\Delta H = -8.36$ W m$^{-2}$ or $-11.3\%$; $\Delta \lambda E = -3.12$ W m$^{-2}$ or $-2.1\%$) during summer. Using the same model domain and season, we find similar patterns ($\Delta H = -4.21$ W m$^{-2}$ or $-7.5\%$ and $\Delta \lambda E = -0.63$ W m$^{-2}$ or $-0.8\%$), though the magnitude of change is lower in our study, which could be due to both the different land-surface model used and the lower value of direct shortwave radiative effect ($-16$ W m$^{-2}$ in Matsui et al., 2008 vs.

$-6.4$ W m$^{-2}$ in present study). Davin and Seneviratne (2012) found that a higher and more realistic diffuse fraction $k_d$ improves the prediction of summertime $T_s$ over Europe than a fixed $k_d$ of 0.30.

Our results highlight the importance of differentiating between total radiative forcing and diffuse radiative forcing at the surface and vegetation responses to these forcings. Currently, $K_{\downarrow,d}$ remains a relatively understudied component of the radiative budget (Halthore & Schwartz, 2000). Although atmospheric reanalysis modeling systems, such as NCEP/NCAR (Kalnay et al., 1996), MERRA-2 (Gelaro et al., 2017), and ERA5 (Hersbach et al., 2020), have gridded $K_{\downarrow,d}$ values, they have not been rigorously evaluated against field observations, which remain scarce. In the Radiative Forcing Model Intercomparison Project, the primary focus is on the quantity of the radiative forcing compared to the pre-industrial baseline, with a tertiary focus on the aerosol radiative forcing (Pincus et al., 2016). Given the importance of the quality of the radiative forcing demonstrated in the present study, we recommend a coordinated effort to compare $K_{\downarrow,d}$ among the models taking part in CMIP6, which would also constrain climate sensitivity to other climate forcers that change $K_{\downarrow,d}$, like clouds (K. Wang et al., 2008). Note that to ensure realistic representation of aerosol impact on $K_{\downarrow,d}$, it is important to compare absorbing versus scattering aerosols as prescribed in or simulated by different models. Even identical AOD values can lead to different $K_{\downarrow,d}$. The presence of primarily absorbing aerosols would reduce both $K_{\downarrow,d}$ and $K_{\downarrow,b}$, while primarily scattering aerosols would reduce $K_{\downarrow,b}$ but enhance $K_{\downarrow,d}$ through forward scattering (Gadhavi & Jayaraman, 2010). The present study gives an evaluation of the CAM6-simulated diffuse radiation at the global scale. Although the model has reproduced the observed spatial variations in $K_{\downarrow,d}$ reasonably well on the global scale and also regionally ($r^2$ 0.92–0.98; Figure S2), its diffuse fraction $k_d$ is biased low due to a high bias in $K_\downarrow$ (Figure S3) and a low bias in $K_{\downarrow,d}$ (Figure S2). For the 224 model grids that contain GEBA observations for both $K_\downarrow$ and $K_{\downarrow,d}$, the modeled $k_d$ is biased low by an average amount of 0.08. In contrast, Mercado et al. (2009) evaluated their modeled $k_d$ using a subset of GEBA observations in Europe, Germany, and China, demonstrating a positive bias in their simulated values for Europe and Germany and comparable values for China. The global land mean $k_d$ (0.34, Run $P$) is lower than the value of $k_d$ for photosynthetically active radiation of 0.41 reported by Ryu et al. (2018). For reference, the global mean $k_d$ is 0.27 for Run $C$. If we assume that the model error in $k_d$ is 0.07 and that this error only affects Run $P$, correcting the model bias would change the diffuse radiation fertilization effect on $\Delta T$ from $-0.007$ K in Figure 7a to $-0.014$ K, which is still much smaller in magnitude than the global dimming effect ($-0.040$ K). In other words, the conclusion that the dimming effect dominates the fertilization effect still holds despite the bias error. Furthermore, most of the error will probably cancel out in the perturbation signal (difference between Run $P$ and $C$) because $k_d$ in Run $C$ is likely biased by a similar amount as both runs incorporate clouds.

On the land-modeling side, there are three broad leaf-to-canopy upscaling schemes (one-big-leaf, two-big-leaf, and multi-layer; Luo et al., 2018). The one-big-leaf models ignore shaded leaves and are thus unable to simulate the diffuse radiation fertilization effect (Lian et al., 2018). On the other hand, CLM uses a two-big-leaf approach for photosynthesis and transpiration, where the carbon and water cycle are separately calculated for sunlit and shaded parts of the canopy, with sunlit leaves receiving both beam radiation and diffuse radiation and shaded leaves receiving only diffuse radiation, and the LAI dependence captured through the fractional change of shaded versus sunlit leaves (Bonan et al., 2011; Kennedy et al., 2019; Oliveira et al., 2011). Of the land surface models (LSMs) taking part in the LUMIP (Lawrence et al., 2016), at least three still use the one-big-leaf scheme (Table 3). Likewise, the land surface modules in regional weather models usually have the simplistic one-big-leaf type representation of the vegetation (Davin & Seneviratne, 2012) or even combined vegetation and ground surface layers (Chakraborty et al., 2019). Thus, regional studies on aerosol impact on the surface energy budget using these models evidently miss this key mechanism (Li et al., 2017; Pere et al., 2011). Improved representation of canopy architecture to resolve the scale mismatch between leaf and canopy leads to more accurate estimation of radiation transfer through the canopy layer and better agreement between simulated and observed GPP in many cases (Bonan et al., 2012). It is important to stress, however, that these evaluations are based on light-response curves and do not explicitly resolve the response of vegetation to $K_{\downarrow,d}$. Uncertainties still remain as to how well the CLM model simulates the GPP response to $K_{\downarrow,d}$ (Wozniak et al., 2020). However, our results are not adversely affected by these uncertainties as the cooling attributed to the diffuse fertilization effect is minor in comparison to the overall Bowen ratio change. Our modeling results regarding the latter are broadly consistent with previous regional (Davin & Seneviratne, 2012; Matsui et al., 2008; Zhang et al., 2008) and global-scale

**Table 3**
*Overview of the Land Surface Models (LSMs) and Their Parent Earth System Models (ESMs) Taking Part in the Land Model Intercomparison Project (LUMIP), and Their Canopy Representation*

| Model | | Overview | | |
|---|---|---|---|---|
| ESM | LSM | Canopy representation | Reference | Additional note |
| CESM2 | CLM5.0 | Two-big-leaf | Lawrence et al. (2019) | Big leaf has one sunlit and one shaded part |
| CMCC-ESM | CLM4.5 | Two-big-leaf | Oleson et al. (2013) | Big leaf has one sunlit and one shaded part |
| CNRM-ESM2 | ISBA-CTRIP | Multi-layer | Carrer et al. (2013) | 10-layer canopy |
| E3SMv1 | ELM (CLM4.5) | Two-big-leaf | Oleson et al. (2013) | Big leaf has one sunlit and one shaded part |
| EC-Earth | LPJ-GUESS | One-big-leaf | Smith et al. (2001) | No shaded leaf |
| GFDL-ESM4 | LM4 | Multi-layer | Weng et al. (2015) | Multi-layer collection of cohort that compete for sunlight |
| GISS | ModelE | Multi-layer | Spitters et al. (1986) | Multi-layer two stream model with direct/diffuse fraction for each layer |
| MIROC-ES2L | Matsiro/VISIT | One-big-leaf | Takata et al. (2003) | No shaded leaf |
| MPI-ESM1.2-LR | JSBACH3.2 | One-big-leaf | Loew et al. (2014) | No shaded leaf |
| NorESM | CLM5.0 | Two-big-leaf | Lawrence et al. (2019) | Big leaf has one sunlit and one shaded part |
| UKESM1-0-LL | JULES-ES-1.0 | Multi-layer | Clark et al. (2011) | Diffuse radiation is fixed as 0.4 of total downwelling in standard configuration; 10-layer canopy |

CLM, Community Land Model.

modeling studies on this topic (Table 1, Liu et al., 2014), as well as several field-scale observational studies (Gu et al., 2002, 2003; Kanniah et al., 2012; Niyogi et al., 2004; K. Wang et al., 2008; S. Wang et al., 2018; W. Wang et al., 2018). On the measurement side, observational constraints on the diffuse radiation fertilization effect are lacking (Steiner et al., 2013). Regions where the magnitude of this signal would be strong, such as heavily polluted tropical areas, have a dearth of simultaneous measurements of $K_{\downarrow,d}$ and the surface energy fluxes—an important issue to address in future studies.

The main limitation of the present study is that the atmosphere is prescribed rather than interactive. In the real world, increases in EF would also lead to local feedback on grid-level forcing variables such as air temperature and humidity and to regional and global feedback via changes in cloud cover and potential changes in aerosol circulation. According to our CLM runs, the local screen-height air temperature is, expectedly, also reduced by aerosols, though the magnitude of decrease is only 0.02 K (global land mean); much smaller than the reduction in surface temperature (mean reduction of 0.13 K; Figure S14). This stronger sensitivity of surface temperature is similar to the local cooling effect of reforestation (Novick & Katul, 2020). In an idealized numerical experiment in which the surface $\lambda E$ is increased by 1 W m$^{-2}$ and $H$ decreased by 1 W m$^{-2}$ uniformly across the land and the ocean surface (equivalent to an increase of EF by 0.014), the global surface temperature is reduced by 0.54 K due to increases in cloudiness (Ban-Weiss et al., 2011). In other words, the non-radiative pathway of aerosols (via EF increase) could lead to additional cooling via a cloud feedback, although the feedback strength may have been overestimated by this idealized experiment because the 1 W m$^{-2}$ addition is applied to $\lambda E$ at all times (in day and night and in growing and non-growing season) and over both the land and the ocean surfaces.

With aerosol emissions expected to decrease in future climate scenarios (Westervelt et al., 2015), better constraining aerosol-biosphere-climate interactions will help us isolate regions vulnerable to future warming. In the context of this study, at the local scale, some of the future warming will result from the decrease in the aerosol surface radiative effect and from the decrease in EF due to global brightening. Based on our results, for the highly populated and highly polluted regions of northern India and eastern China, where roughly

half of the AOD is from anthropogenic sources (Chakraborty & Lee, 2019), the radiative and non-radiative pathways can lead to an additional annual mean warming of 0.3–0.4 K if all anthropogenic aerosols are removed (Figure S12f). In contrast, the geoengineering scenario of injecting aerosols to the stratosphere to offset greenhouse gas warming will change the surface energy budget and temperature in the opposite direction to pollution abatement. One analog for such a scenario is the eruption of Mount Pinatubo in 1991 (Proctor et al., 2018). According to the MERRA-2 reanalysis, this volcanic eruption reduced the global $K_\downarrow$ by about 3.05 W m$^{-2}$ and increased $K_{\downarrow,d}$ by 3.74 W m$^{-2}$ (year 1992s annual mean minus the mean of 1988–1990), or about one-third of the aerosol surface radiative forcing shown in Figure 3. A similar amount of $K_{\downarrow,d}$ increase is reported from a global model simulation of stratospheric sulphate geoengineering (3.20 W m$^{-2}$; Xia et al., 2016). These results suggest that aerosols from geoengineering will have a modest non-radiative effect on local temperature.

## 5. Conclusions

We develop a modeling framework for understanding terrestrial aerosol-climate interactions from the surface energy budget perspective. In this framework, aerosols reduce the incoming shortwave radiation four times as much as they increase the incoming longwave radiation, with an overall reduction in the incoming radiation energy of 6.60 W m$^{-2}$ over the global terrestrial surface. Our modeling results demonstrate that the reduction in the incoming radiation is mainly compensated by a reduction in the surface sensible heat flux ($\Delta H = -3.59$ W m$^{-2}$) and to a lesser extent by a reduction in the surface evaporation ($\Delta \lambda E = -0.51$ W m$^{-2}$), leading to an increase in the terrestrial evaporation fraction EF by 0.023. The main mechanism for the EF increase is change in energy allocation due to global dimming (reduction in incoming solar radiation) and augmented by a diffuse radiation fertilization effect or enhanced transpiration from the shaded plant canopy due to the increase of diffuse radiation. We then partition the surface temperature response into contributions from the radiative pathway (reduction in incoming radiation energy) and from the non-radiative pathway (increase in EF). A surprising result is that for grids with LAI > 2, the non-radiative pathway dominates the local temperature response over the radiative pathway. The diffuse radiation fertilization effect alone has a small effect on the terrestrial surface energy budget, increasing evaporation by 0.18 W m$^{-2}$ or 0.48% of total terrestrial evaporation. This contrasts sharply with the terrestrial carbon budget response, with the diffuse radiation fertilization increasing GPP by a much larger amount of 2.18 Pg C y$^{-1}$ or 1.8% of the total GPP. Given the model-dependent nature of the magnitude of some of these results, we discuss the importance of comprehensive future land model evaluations focused on the diffuse radiation fertilization effect.

## Data Availability Statement

The Community Earth System Model is a public domain software and its releases are accessible through this GitHub repository: https://github.com/ESCOMP/CESM. The MERRA-2 reanalysis dataset can be found on NASA's website (https://gmao.gsfc.nasa.gov/reanalysis/MERRA-2/). The GSWP3 data used in this study was accessed through NCAR's Globally Accessible Data Environment, but can also be accessed through the Inter-Sectoral Impact Model Intercomparison Project Earth System Grid Federation server (https://www.isimip.org/gettingstarted/input-data-bias-correction/details/4/).The GEBA and FLUXCOM datasets can be accessed from their respective websites (https://geba.ethz.ch/and http://www.fluxcom.org/). The CABLE source code can be accessed through NCI (https://trac.nci.org.au/trac/cable/wiki/CableRegistration). Other datasets used and generated for this study, as well as the codes used for data analysis and modifying the model outputs are available from the authors upon reasonable request.

## References

Ban-Weiss, G. A., Bala, G., Cao, L., Pongratz, J., & Caldeira, K. (2011). Climate forcing and response to idealized changes in surface latent and sensible heat. *Environmental Research Letters*, *6*(3), 034032. https://doi.org/10.1088/1748-9326/6/3/034032

Bonan, G. B. (2008). Forests and climate change: Forcings, feedbacks, and the climate benefits of forests. *Science*, *320*, 1444–1449. https://doi.org/10.1126/science.1155121

Bonan, G. B., Lawrence, P. J., Oleson, K. W., Levis, S., Jung, M., Reichstein, M., et al. (2011). Improving canopy processes in the community land model version 4 (CLM4) using global flux fields empirically inferred from FLUXNET data. *Journal of Geophysical Research*, *116*(G2). https://doi.org/10.1029/2010jg001593

Bonan, G. B., Oleson, K. W., Fisher, R. A., Lasslop, G., & Reichstein, M. (2012). Reconciling leaf physiological traits and canopy flux data: Use of the TRY and FLUXNET databases in the Community Land Model version 4. *Journal of Geophysical Research*, *117*(G2). https://doi.org/10.1029/2011jg001913

Bright, R. M., Davin, E., O'Halloran, T., Pongratz, J., Zhao, K., & Cescatti, A. (2017). Local temperature response to land cover and management change driven by non-radiative processes. *Nature Climate Change*, *7*, 296–302. https://doi.org/10.1038/nclimate3250

Burakowski, E., Tawfik, A., Ouimette, A., Lepine, L., Novick, K., Ollinger, S., et al. (2018). The role of surface roughness, albedo, and Bowen ratio on ecosystem energy balance in the Eastern United States. *Agricultural and Forest Meteorology*, *249*, 367–376. https://doi.org/10.1016/j.agrformet.2017.11.030

Carrer, D., Roujean, J.-L., Lafont, S., Calvet, J.-C., Boone, A., Decharme, B., et al. (2013). A canopy radiative transfer scheme with explicit FAPAR for the interactive vegetation model ISBA-A-gs: Impact on carbon fluxes. *Journal of Geophysical Research: Biogeosciences*, *118*(2), 888–903. https://doi.org/10.1002/jgrg.20070

Chakraborty, T., & Lee, X. (2019). Land cover regulates the spatial variability of temperature response to the direct radiative effect of aerosols. *Geophysical Research Letters*, *46*(15), 8995–9003. https://doi.org/10.1029/2019gl083812

Chakraborty, T., Sarangi, C., Krishnan, M., Tripathi, S. N., Morrison, R., & Evans, J. (2019). Biases in model-simulated surface energy fluxes during the Indian monsoon onset period. *Boundary-Layer Meteorology*, *170*(2), 323–348. https://doi.org/10.1007/s10546-018-0395-x

Chakraborty, T., Sarangi, C., & Lee, X. (2021). Reduction in human activity can enhance the urban heat island: Insights from the COVID-19 lockdown. *Environmental Research Letters*. https://doi.org/10.1088/1748-9326/abef8e

Chen, M., & Zhuang, Q. (2014). Evaluating aerosol direct radiative effects on global terrestrial ecosystem carbon dynamics from 2003 to 2010. *Tellus B: Chemical and Physical Meteorology*, *66*(1), 21808. https://doi.org/10.3402/tellusb.v66.21808

Chung, C. E., Ramanathan, V., Kim, D., & Podgorny, I. A. (2005). Global anthropogenic aerosol direct forcing derived from satellite and ground-based observations. *Journal of Geophysical Research*, *110*(D24). https://doi.org/10.1029/2005JD006356

Clark, D. B., Mercado, L. M., Sitch, S., Jones, C. D., Gedney, N., Best, M. J., et al. (2011). The joint UK land environmentsSimulator (JULES), model description—Part 2: Carbon fluxes and vegetation dynamics. *Geoscientific Model Development*, *4*(3), 701–722. https://doi.org/10.5194/gmd-4-701-2011

Dai, Y., Dickinson, R. E., & Wang, Y.-P. (2004). A two-big-leaf model for canopy temperature, photosynthesis, and stomatal conductance. *Journal of Climate*, *17*(12), 2281–2299. https://doi.org/10.1175/1520-0442(2004)017<2281:atmfct>2.0.co10.1175/1520-0442(2004)017<2281:atmfct>2.0.co;2

Davin, E. L., & Seneviratne, S. I. (2012). Role of land surface processes and diffuse/direct radiation partitioning in simulating the European climate. *Biogeosciences*, *9*(5), 1695–1707. https://doi.org/10.5194/bg-9-1695-2012

Dirmeyer, P. A. (2011). A history and review of the global soil wetness project (GSWP). *Journal of Hydrometeorology*, *12*(5), 729–749. https://doi.org/10.1175/jhm-d-10-05010.1

Gadhavi, H., & Jayaraman, A. (2010). Absorbing aerosols: Contribution of biomass burning and implications for radiative forcing. *Annales Geophysicae*, *28*, 103–111. https://doi.org/10.5194/angeo-28-103-2010

Gelaro, R., McCarty, W., Suárez, M. J., Todling, R., Molod, A., Takacs, L., et al. (2017). The modern-era retrospective analysis for research and applications, version 2 (MERRA-2). *Journal of Climate*, *30*(14), 5419–5454. https://doi.org/10.1175/JCLI-D-16-0758.1

Gettelman, A., Mills, M. J., Kinnison, D. E., Garcia, R. R., Smith, A. K., Marsh, D. R., et al. (2019). The whole atmosphere community climate model version 6 (WACCM6). *Journal of Geophysical Research: Atmospheres*, *124*(23), 12380–12403. https://doi.org/10.1029/2019jd030943

Gu, L., Baldocchi, D. D., Wofsy, S. C., Munger, J. W., Michalsky, J. J., Urbanski, S. P., & Boden, T. A. (2003). Response of a deciduous forest to the Mount Pinatubo eruption: Enhanced photosynthesis. *Science*, *299*(5615), 2035–2038. https://doi.org/10.1126/science.1078366

Gu, L., Baldocchi, D., Verma, S. B., Black, T. A., Vesala, T., Falge, E. M., & Dowty, P. R. (2002). Advantages of diffuse radiation for terrestrial ecosystem productivity. *Journal of Geophysical Research*, *107*(D6), 1–23. https://doi.org/10.1029/2001jd001242

Gu, L., Meyers, T., Pallardy, S. G., Hanson, P. J., Yang, B., Heuer, M., et al. (2006). Direct and indirect effects of atmospheric conditions and soil moisture on surface energy partitioning revealed by a prolonged drought at a temperate forest site. *Journal of Geophysical Research*, *111*(D16). https://doi.org/10.1029/2006jd007161

Halthore, R. N., & Schwartz, S. E. (2000). Comparison of model-estimated and measured diffuse downward irradiance at surface in cloud-free skies. *Journal of Geophysical Research*, *105*(D15), 20165–20177. https://doi.org/10.1029/2000jd900224

Hersbach, H., Bell, B., Berrisford, P., Hirahara, S., Horányi, A., Muñoz-Sabater, J., et al. (2020). The ERA5 global reanalysis. *Quarterly Journal of the Royal Meteorological Society*, *146*(730), 1999–2049. https://doi.org/10.1002/qj.3803

Hinds, W. C. (1999). *Aerosol technology: Properties, behavior, and measurement of airborne particles*. Wiley.

Jung, M., Koirala, S., Weber, U., Ichii, K., Gans, F., Camps-Valls, G., et al. (2019). The FLUXCOM ensemble of global land-atmosphere energy fluxes. *Scientific Data*, *6*(1), 1–14. https://doi.org/10.1038/s41597-019-0076-8

Kalnay, E., Kanamitsu, M., Kistler, R., Collins, W., Deaven, D., Gandin, L., et al. (1996). The NCEP/NCAR 40-year reanalysis project. *Bulletin of the American Meteorological Society*, *77*(3), 437–472. https://doi.org/10.1175/1520-0477(1996)077<0437:tnyrp>2.0.co;2

Kanniah, K. D., Beringer, J., North, P., & Hutley, L. (2012). Control of atmospheric particles on diffuse radiation and terrestrial plant productivity. *Progress in Physical Geography: Earth and Environment*, *36*(2), 209–237. https://doi.org/10.1177/0309133311434244

Kennedy, D., Swenson, S., Oleson, K. W., Lawrence, D. M., Fisher, R., Lola da Costa, A. C., & Gentine, P. (2019). Implementing plant hydraulics in the community land model, version 5. *Journal of Advances in Modeling Earth Systems*, *11*(2), 485–513. https://doi.org/10.1029/2018ms001500

Knohl, A., & Baldocchi, D. D. (2008). Effects of diffuse radiation on canopy gas exchange processes in a forest ecosystem. *Journal of Geophysical Research*, *113*(G2). https://doi.org/10.1029/2007jg000663

Knyazikhin, Y., Martonchik, J. V., Myneni, R. B., Diner, D. J., & Running, S. W. (1998). Synergistic algorithm for estimating vegetation canopy leaf area index and fraction of absorbed photosynthetically active radiation from MODIS and MISR data. *Journal of Geophysical Research*, *103*(D24), 32257–32275. https://doi.org/10.1029/98JD02462

Kowalczyk, E. A., Wang, Y. P., Law, R. M., Davies, H. L., McGregor, J. L., & Abramowitz, G. (2006). *The CSIRO Atmosphere Biosphere Land Exchange (CABLE) model for use in climate models and as an offline model*. CSIRO Marine and Atmospheric Research. https://doi.org/10.4225/08/58615c6a9a51d

Lawrence, D. M., Fisher, R. A., Koven, C. D., Oleson, K. W., Swenson, S. C., Bonan, G., & Zeng, X. (2019). The Community Land Model version 5: Description of new features, benchmarking, and impact of forcing uncertainty. *Journal of Advances in Modeling Earth Systems*, *11*(12), 4245–4287. https://doi.org/10.1029/2018MS001583

Lawrence, D. M., Hurtt, G. C., Arneth, A., Brovkin, V., Calvin, K. V., Jones, A. D., et al. (2016). The land use model intercomparison project (LUMIP) contribution to CMIP6: Rationale and experimental design. *Geoscientific Model Development*, *9*(9), 2973–2998. https://doi.org/10.5194/gmd-9-2973-2016

Lee, X., Goulden, M. L., Hollinger, D. Y., Barr, A., Black, T. A., Bohrer, G., et al. (2011). Observed increase in local cooling effect of deforestation at higher latitudes. *Nature*, *479*(7373), 384–387. https://doi.org/10.1038/nature10588

Li, M., Wang, T., Xie, M., Zhuang, B., Li, S., Han, Y., & Chen, P. (2017). Impacts of aerosol-radiation feedback on local air quality during a severe haze episode in Nanjing megacity, eastern China. *Tellus B: Chemical and Physical Meteorology*, *69*(1), 1339548. https://doi.org/10.1080/16000889.2017.1339548

Lian, X., Piao, S., Huntingford, C., Li, Y., Zeng, Z., Wang, X., et al. (2018). Partitioning global land evapotranspiration using CMIP5 models constrained by observations. *Nature Climate Change*, *8*(7), 640–646. https://doi.org/10.1038/s41558-018-0207-9

Liu, S., Chen, M., & Zhuang, Q. (2014). Aerosol effects on global land surface energy fluxes during 2003–2010. *Geophysical Research Letters*, *41*(22), 7875–7881. https://doi.org/10.1002/2014gl061640

Loew, A., Van Bodegom, P. M., Widlowski, J.-L., Otto, J., Quaife, T., Pinty, B., & Raddatz, T. (2014). Do we (need to) care about canopy radiation schemes in DGVMs? Caveats and potential impacts. *Biogeosciences*, *11*(7), 1873–1897. https://doi.org/10.5194/bg-11-1873-2014

Lu, X., Chen, M., Liu, Y., Miralles, D. G., & Wang, F. (2017). Enhanced water use efficiency in global terrestrial ecosystems under increasing aerosol loadings. *Agricultural and Forest Meteorology*, *237–238*, 39–49. https://doi.org/10.1016/j.agrformet.2017.02.002

Luo, X., Chen, J. M., Liu, J., Black, T. A., Croft, H., Staebler, R., et al. (2018). Comparison of big-leaf, two-big-leaf, and two-leaf upscaling schemes for evapotranspiration estimation using coupled carbon-water modeling. *Journal of Geophysical Research: Biogeosciences*, *123*(1), 207–225. https://doi.org/10.1002/2017JG003978

Luyssaert, S., Jammet, M., Stoy, P. C., Estel, S., Pongratz, J., Ceschia, E., et al. (2014). Land management and land-cover change have impacts of similar magnitude on surface temperature. *Nature Climate Change*, *4*(5), 389–393. https://doi.org/10.1038/nclimate2196.

Lyapustin, A., Wang, Y., Korkin, S., & Huang, D. (2018). MODIS collection 6 MAIAC algorithm. *Atmospheric Measurement Techniques*, *11*(10), 5741–5765. https://doi.org/10.5194/amt-11-5741-2018

Matsui, T., Beltrán-Przekurat, A., Niyogi, D., Pielke, R. A., & Coughenour, M. (2008). Aerosol light scattering effect on terrestrial plant productivity and energy fluxes over the eastern United States. *Journal of Geophysical Research*, *113*(D14). https://doi.org/10.1029/2007jd009658

Mercado, L. M., Bellouin, N., Sitch, S., Boucher, O., Huntingford, C., Wild, M., & Cox, P. M. (2009). Impact of changes in diffuse radiation on the global land carbon sink. *Nature*, *458*, 1014–1017. https://doi.org/10.1038/nature07949

Niyogi, D., Chang, H. I., Saxena, V. K., Holt, T., Alapaty, K., Booker, F., & Xue, Y. (2004). Direct observations of the effects of aerosol loading on net ecosystem $CO_2$ exchanges over different landscapes. *Geophysical Research Letters*, *31*(20). https://doi.org/10.1029/2004gl020915

Novick, K. A., & Katul, G. G. (2020). The duality of reforestation impacts on surface and air temperature. *Journal of Geophysical Research: Biogeosciences*, *125*(4), e2019JG005543. https://doi.org/10.1029/2019jg005543

Oleson, K. W., Lawrence, D. M., Bonan, G. B., Drewniak, B., Huang, M., Koven, C. D., & Thornton, P. E. (2013). Technical description of version 4.5 of the Community Land Model (CLM) (No. NCAR/TN-503+STR). https://doi.org/10.5065/D6RR1W7M

Oliveira, P. J. C., Davin, E. L., Levis, S., & Seneviratne, S. I. (2011). Vegetation-mediated impacts of trends in global radiation on land hydrology: A global sensitivity study. *Global Change Biology*, *17*, 3453–3467. https://doi.org/10.1111/j.1365-2486.2011.02506.x

Panicker, A. S., Pandithurai, G., Safai, P. D., & Kewat, S. (2008). Observations of enhanced aerosol longwave radiative forcing over an urban environment. *Geophysical Research Letters*, *35*(4). https://doi.org/10.1029/2007gl032879

Péré, J. C., Mallet, M., Pont, V., & Bessagnet, B. (2011). Impact of aerosol direct radiative forcing on the radiative budget, surface heat fluxes, and atmospheric dynamics during the heat wave of summer 2003 over western Europe: A modeling study. *Journal of Geophysical Research*, *116*(D23). https://doi.org/10.1029/2011jd016240

Persad, G. G., & Caldeira, K. (2018). Divergent global-scale temperature effects from identical aerosols emitted in different regions. *Nature Communications*, *9*(1), 1–9. https://doi.org/10.1038/s41467-018-05838-6

Pincus, R., Forster, P. M., & Stevens, B. (2016). The radiative forcing model intercomparison project (RFMIP): Experimental protocol for CMIP6. *Geoscientific Model Development*, *9*(9), 3447–3460. https://doi.org/10.5194/gmd-9-3447-2016

Proctor, J., Hsiang, S., Burney, J., Burke, M., & Schlenker, W. (2018). Estimating global agricultural effects of geoengineering using volcanic eruptions. *Nature*, *560*(7719), 480–483. https://doi.org/10.1038/s41586-018-0417-3

Ramanathan, V. (2001). Aerosols, climate, and the hydrological cycle. *Science*, *294*, 2119–2124. https://doi.org/10.1126/science.1064034

Rap, A., Scott, C. E., Reddington, C. L., Mercado, L., Ellis, R. J., Garraway, S., et al. (2018). Enhanced global primary production by biogenic aerosol via diffuse radiation fertilization. *Nature Geoscience*, *11*(9), 640–644. https://doi.org/10.1038/s41561-018-0208-3

Rap, A., Spracklen, D. V., Mercado, L., Reddington, C. L., Haywood, J. M., Ellis, R. J., et al. (2015). Fires increase Amazon forest productivity through increases in diffuse radiation. *Geophysical Research Letters*, *42*(11), 4654–4662. https://doi.org/10.1002/2015gl063719

Rubel, F., & Kottek, M. (2010). Observed and projected climate shifts 1901–2100 depicted by world maps of the Köppen-Geiger climate classification. *Meteorologische Zeitschrift*, *19*(2), 135–141. https://doi.org/10.1127/0941-2948/2010/0430

Ruehr, S., Lee, X., Smith, R., Li, X., Xu, Z., Liu, S., et al. (2020). A mechanistic investigation of the oasis effect in the Zhangye cropland in semiarid western China. *Journal of Arid Environments*, *176*, 104120. https://doi.org/10.1016/j.jaridenv.2020.104120

Ryu, Y., Jiang, C., Kobayashi, H., & Detto, M. (2018). MODIS-derived global land products of shortwave radiation and diffuse and total photosynthetically active radiation at 5 km resolution from 2000. *Remote Sensing of Environment*, *204*, 812–825. https://doi.org/10.1016/j.rse.2017.09.021

Smith, B., Prentice, I. C., & Sykes, M. T. (2001). Representation of vegetation dynamics in the modeling of terrestrial ecosystems: Comparing two contrasting approaches within European climate space. *Global Ecology and Biogeography*, *10*, 621–637. https://doi.org/10.1046/j.1466-822X.2001.t01-1-00256.x10.1046/j.1466-822x.2001.00256.x

Spitters, C. J. T., Toussaint, H. A. J. M., & Goudriaan, J. (1986). Separating the diffuse and direct component of global radiation and its implications for modeling canopy photosynthesis. Part I. Components of incoming radiation. *Agricultural and Forest Meteorology*, *38*(1–3), 217–229. https://doi.org/10.1016/0168-1923(86)90060-2

Steiner, A. L., Mermelstein, D., Cheng, S. J., Twine, T. E., & Oliphant, A. (2013). Observed impact of atmospheric aerosols on the surface energy budget. *Earth Interactions*, *17*(14), 1–22. https://doi.org/10.1175/2013ei000523.1

Stocker, T. (2014). *Climate change 2013: The physical science basis: Working Group I contribution to the fifth assessment report of the Intergovernmental panel on climate change*. Cambridge University Press. https://doi.org/10.1017/CBO9781107415324

Takata, K., Emori, S., & Watanabe, T. (2003). Development of the minimal advanced treatments of surface interaction and runoff. *Global and Planetary Change*, *38*(1–2), 209–222. https://doi.org/10.1016/S0921-8181(03)00030-4

Talukdar, S., Venkat Ratnam, M., Ravikiran, V., & Chakraborty, R. (2019). Influence of black carbon aerosol on the atmospheric instability. *Journal of Geophysical Research: Atmospheres*, *124*(10), 5539–5554. https://doi.org/10.1029/2018JD029611

Wang, K., Dickinson, R. E., & Liang, S. (2008). Observational evidence on the effects of clouds and aerosols on net ecosystem exchange and evapotranspiration. *Geophysical Research Letters*, *35*(10). https://doi.org/10.1029/2008gl034167

Wang, S., Ibrom, A., Bauer-Gottwein, P., & Garcia, M. (2018). Incorporating diffuse radiation into a light use efficiency and evapotranspiration model: An 11-year study in a high latitude deciduous forest. *Agricultural and Forest Meteorology*, *248*, 479–493. https://doi.org/10.1016/j.agrformet.2017.10.023

Wang, W., Lee, X., Xiao, W., Liu, S., Schultz, N., Wang, Y., et al. (2018). Global lake evaporation accelerated by changes in surface energy allocation in a warmer climate. *Nature Geoscience*, *11*(6), 410–414. https://doi.org/10.1038/s41561-018-0114-8

Wang, Y., Xia, W., Liu, X., Xie, S., Lin, W., Tang, Q., et al. (2021). Disproportionate control on aerosol burden by light rain. *Nature Geoscience*, *14*(2), 72–76. https://doi.org/10.1038/s41561-020-00675-z

Wang, Y. P., & Leuning, R. (1998). A two-leaf model for canopy conductance, photosynthesis and partitioning of available energy. I: Model description and comparison with a multi-layered model. *Agricultural and Forest Meteorology*, *91*(1–2), 89–111. https://doi.org/10.1016/s0168-1923(98)00061-6

Weng, E. S., Malyshev, S., Lichstein, J. W., Farrior, C. E., Dybzinski, R., Zhang, T., et al. (2015). Scaling from individual trees to forests in an Earth system modeling framework using a mathematically tractable model of height-structured competition. *Biogeosciences*, *12*(9), 2655–2694. https://doi.org/10.5194/bg-12-2655-2015

Westervelt, D. M., Horowitz, L. W., Naik, V., Golaz, J.-C., & Mauzerall, D. L. (2015). Radiative forcing and climate response to projected 21st century aerosol decreases. *Atmospheric Chemistry and Physics*, *15*(22), 12681–12703. https://doi.org/10.5194/acp-15-12681-2015

Wild, M., Ohmura, A., Schär, C., Müller, G., Folini, D., Schwarz, M., et al. (2017). The Global Energy Balance Archive (GEBA) version 2017: A database for worldwide measured surface energy fluxes. *Earth System Science Data*, *9*(2), 601–613. https://doi.org/10.5194/essd-9-601-2017

Wozniak, M. C., Bonan, G. B., Keppel-Aleks, G., & Steiner, A. L. (2020). Influence of vertical heterogeneities in the canopy microenvironment on interannual variability of carbon uptake in temperate deciduous forests. *Journal of Geophysical Research: Biogeosciences*, *125*(8), e2020JG005658. https://doi.org/10.1029/2020jg005658

Xia, L., Robock, A., Tilmes, S., & Neely, R. R., Iii (2016). Stratospheric sulphate geoengineering could enhance the terrestrial photosynthesis rate. *Atmospheric Chemistry and Physics*, *16*(3), 1479–1489. https://doi.org/10.5194/acp-16-1479-2016

Yue, X., & Unger, N. (2018). Fire air pollution reduces global terrestrial productivity. *Nature Communications*, *9*(1), 1–9. https://doi.org/10.1038/s41467-018-07921-4

Zhang, Y., Fu, R., Yu, H., Dickinson, R. E., Juarez, R. N., Chin, M., & Wang, H. (2008). A regional climate model study of how biomass burning aerosol impacts land-atmosphere interactions over the Amazon. *Journal of Geophysical Research*, *113*(D14). https://doi.org/10.1029/2007jd009449

Zhao, L., Lee, X., Smith, R. B., & Oleson, K. (2014). Strong contributions of local background climate to urban heat islands. *Nature*, *511*(7508), 216–219. https://doi.org/10.1038/nature13462